Revisiting the blocking force test on ferroelectric ceramics using high energy x-ray diffraction

L. Daniel,[1,2,a)] D. A. Hall,[1] J. Koruza,[3] K. G. Webber,[3] A. King,[4,5] and P. J. Withers[1]

[1]*School of Materials, University of Manchester, Manchester M13 9PL, United Kingdom*
[2]*GeePs (CNRS UMR8507, CentraleSupelec, UPMC, Univ Paris-Sud), 91192 Gif sur Yvette cedex, France*
[3]*Institute of Materials Science, Technische Universität Darmstadt, Alarich-Weiss-Straße 2, 64287 Darmstadt, Germany*
[4]*European Synchrotron Radiation Facility (ESRF), 6 rue J. Horowitz, 38043 Grenoble, France*
[5]*Synchrotron SOLEIL, BP 48, 91192 Gif sur Yvette cedex, France*

The blocking force test is a standard test to characterise the properties of piezoelectric actuators. The aim of this study is to understand the various contributions to the macroscopic behaviour observed during this experiment that involves the intrinsic piezoelectric effect, ferroelectric domain switching, and internal stress development. For this purpose, a high energy diffraction experiment is performed *in-situ* during a blocking force test on a tetragonal lead zirconate titanate (PZT) ceramic $(Pb_{0.98}Ba_{0.01}(Zr_{0.51}Ti_{0.49})_{0.98}Nb_{0.02}O_3)$. It is shown that the usual macroscopic linear interpretation of the test can also be performed at the single crystal scale, allowing the identification of local apparent piezoelectric and elastic properties. It is also shown that despite this apparent linearity, the blocking force test involves significant non-linear behaviour mostly due to domain switching under electric field and stress. Although affecting a limited volume fraction of the material, domain switching is responsible for a large part of the macroscopic strain and explains the high level of inter- and intra-granular stresses observed during the course of the experiment. The study shows that if apparent piezoelectric and elastic properties can be identified for PZT single crystals from blocking stress curves, they may be very different from the actual properties of polycrystalline materials due to the multiplicity of the physical mechanisms involved. These apparent properties can be used for macroscopic modelling purposes but should be considered with caution if a local analysis is aimed at. © 2015 Author(s). All article content, except where otherwise noted, is licensed under a Creative Commons Attribution 3.0 Unported License.
[http://dx.doi.org/10.1063/1.4918928]

I. INTRODUCTION

Piezoelectric ceramics are widely used as the basis for electromechanical sensors and actuators for control, medical, electronic, and micro-electromechanical systems (MEMS) applications. Electromechanical actuators exploit the electric field-induced strain, which can be represented by the linear converse piezoelectric effect.[1] Piezoelectric ceramics are used in many complex electromechanical systems. Their response is a function of the applied electric field but also depends on the mechanical response of the surrounding system. Blocking force curves are a convenient tool in designing actuating systems thereby providing an indication of their limiting behaviour in operation.[2] The interpretation of blocking force measurements is usually carried out on the basis of linear piezoelectricity and elasticity, allowing the identification of the piezoelectric longitudinal coefficient and the Young's modulus. However, it is known that the macroscopic strain of ferroelectric ceramics under electromechanical loading conditions is the result of a complex combination of the intrinsic piezoelectric effect, the extrinsic effects resulting from non-180° domain switching, and the development of internal inter-granular stresses.[3,4] In recent years,

diffraction techniques have been exploited as a means of evaluating the local lattice strain and domain switching behaviour of polycrystalline ferroelectric materials in response to external electric and/or mechanical loading.[3–14] These studies have shed new light on ferroelectric behaviour and enabled the origins of non-linearities to be characterised.

The present paper presents the results of an *in-situ* synchrotron x-ray diffraction (XRD) study on a tetragonal lead zirconate titanate (PZT) ceramic under combined electrical and mechanical loading (composition referred to as PZT 51-49: $Pb_{0.98}Ba_{0.01}(Zr_{0.51}Ti_{0.49})_{0.98}Nb_{0.02}O_3$). Although much research has been conducted to find alternative lead-free compositions, PZT still represents the dominant piezo-ceramic in commercial applications. Although it is known that non-180° domain switching plays an important role in determining the electromechanical behaviour of actuator materials under stress,[15] it is only recently that *in-situ* measurements of blocking stress curves by diffraction methods have been reported.[14] This latter study was conducted on a rhombohedral composition. This paper takes a closer look at the blocking force test, and particularly its linear interpretation, using a high energy diffraction experiment. In the first part, the standard macroscopic interpretation of the blocking force test is recalled. The measurements obtained by synchrotron diffraction *in-situ* during a series of blocking force

a)Author to whom correspondence should be addressed. Electronic mail: laurent.daniel@u-psud.fr

117, 174104-1

tests are presented and discussed. A linear interpretation of this experiment is first proposed, allowing the identification of apparent local piezoelectric and elastic coefficients. The origins of non-linearity are then thoroughly discussed.

II. MACROSCOPIC INTERPRETATION OF THE BLOCKING FORCE TEST

Piezoelectric devices are frequently used under combined electrical and mechanical loading, for example, in high power acoustic transducers and multilayer stack actuators. In the case of actuators, the performance of a device in the presence of a restraining force or static stress can be characterised by measuring the so-called blocking stress relationship.[16] The blocking force test is performed on a poled piezoelectric material and usually interpreted using the standard equations of piezoelectricity (1), where ε, σ, $\mathbf{E}$, and $\mathbf{D}$ are the strain, stress, electric field, and electric displacement, respectively, and $\mathcal{S}^E$, ϵ^σ, and $\mathbf{d}$ are the elastic stiffness tensor at constant electric field, dielectric permittivity at constant stress, and piezoelectric tensor, respectively

$$\begin{cases} \varepsilon_{ij} = S^E_{ijkl}\,\sigma_{kl} + \mathrm{d}_{kij}\,E_k \\ D_i = \mathrm{d}_{ikl}\,\sigma_{kl} + \epsilon^\sigma_{ik}\,E_k. \end{cases} \quad (1)$$

The experimental sequence is conducted according to the so-called direct blocking force method[2] as illustrated in Fig. 1(a). The experiment starts at the reference zero strain. An electric field $\mathbf{E}$ (magnitude E, $\mathbf{E} = (0,0,E)$) is applied first along the macroscopic polarisation direction. Assuming that the piezoelectric behaviour is characterised by three independent coefficients d_{33}, d_{31}, and d_{15} (using Voigt notation: $[d_{33}, d_{31}, d_{15}] = [\mathrm{d}_{333}, \mathrm{d}_{311}, \mathrm{d}_{131}]$), and according to (1) (with $\sigma_{kl} = 0$), the corresponding strain ε^E is given by the following equation:

$$\varepsilon^E = \begin{pmatrix} d_{31}\,E & 0 & 0 \\ 0 & d_{31}\,E & 0 \\ 0 & 0 & d_{33}\,E \end{pmatrix}. \quad (2)$$

Maintaining the electric field $\mathbf{E}$ constant, a compressive stress σ (magnitude σ) is then progressively applied along the same direction as the polarisation and electric field. Assuming an isotropic elastic behaviour, characterized by Young's modulus Y and Poisson's ratio ν, and according to (1), the corresponding strain $\varepsilon^{E\sigma}$ is given by the following equation:

$$\varepsilon^{E\sigma} = \begin{pmatrix} d_{31}\,E - \nu\dfrac{\sigma}{Y} & 0 & 0 \\ 0 & d_{31}\,E - \nu\dfrac{\sigma}{Y} & 0 \\ 0 & 0 & d_{33}\,E + \dfrac{\sigma}{Y} \end{pmatrix}. \quad (3)$$

The blocking stress σ^{BF} is defined for a given intensity E of the electric field as the amplitude of the compressive stress required to cancel the longitudinal strain

$$\sigma^{BF} = -d_{33}\,E\,Y. \quad (4)$$
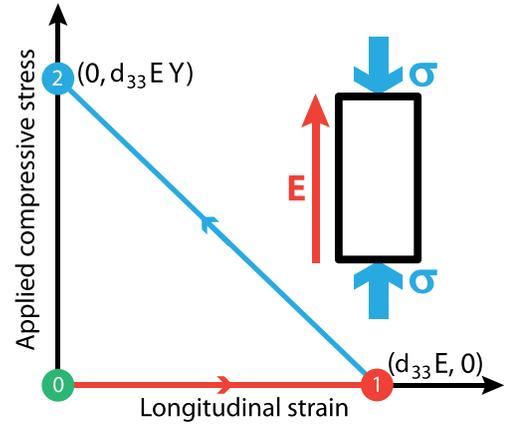
(a) Blocking stress curve
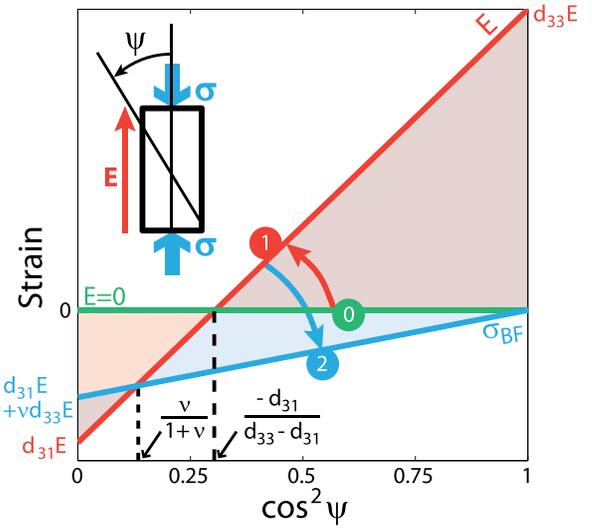
(b) Azimuthal strain

FIG. 1. Principle of the direct blocking force test: (a) Blocking stress curve: Relationship between macroscopic strain and stress. From the poled state ⓪, an electric field E is applied along the macroscopic polarisation direction giving state ①; then a mechanical load is applied along the polarisation direction to reduce the strain to zero giving state ②. (b) Azimuthal strain: The macrostrain as a function of angle to the polarisation direction for the three states ⓪, ①, ② shown in (a). For step ①, the direction with $\cos^2\psi = -d_{31}/(d_{33} - d_{31})$ shows no strain. After step ②, the longitudinal strain is reduced to zero for the blocking stress $\sigma^{BF} = -d_{33}YE$. During the application of stress, the direction with $\cos^2\psi = \nu/(1+\nu)$ shows an unchanged strain.

It is interesting to consider the strain not only in the direction of the polarisation but also as a function of the azimuthal angle ψ, where $\psi = 0$ is the polarisation direction (see Fig. 1(b)). The projection of the strain along a direction $\mathbf{u}_\psi$ is initially zero for all ψ (zero strain reference state). After application of the electric field, the projection of the strain tensor ε^E (2) along $\mathbf{u}_\psi$ is a linear function of $\cos^2\psi$

$$\varepsilon^E(\psi) = {}^t\mathbf{u}_\psi.\varepsilon^E.\mathbf{u}_\psi = (d_{33} - d_{31})\,E\cos^2\psi + d_{31}\,E. \quad (5)$$

The coefficient d_{33} can be directly identified from the measurement of the longitudinal strain ($\psi = 0$, $d_{33} = \varepsilon^E(0°)/E$) and the coefficient d_{31} from the measurement of the transverse strain ($\psi = 90°$, $d_{33} = \varepsilon^E(90°)/E$). The direction ψ^E_0 along which no piezoelectric strain is measured is given by $\cos^2\psi^E_0 = -d_{31}/(d_{33} - d_{31})$ and is independent of the

electric field level. During the application of the compressive stress, the projection becomes

$$\varepsilon^{E\sigma}(\psi) = \left((d_{33} - d_{31})E + \frac{1+\nu}{Y}\sigma \right)\cos^2\psi$$
$$+ \left(d_{31}E - \frac{\nu}{Y}\sigma \right). \quad (6)$$

The direction ψ_0^σ along which the strain is unchanged by the application of the compressive stress is given by $\cos^2\psi_0^\sigma = \nu/(1+\nu)$ and is independent of the magnitude of stress and electric field. When the stress magnitude reaches the blocking stress σ^{BF} (4), the longitudinal strain $\varepsilon_\parallel^{E\sigma}(\psi = 0, \cos^2\psi = 1)$ is reduced to zero, but the transverse strain $\varepsilon_\perp^{E\sigma}(\psi = 90°, \cos^2\psi = 0)$ is not, as expressed in the following equation:

$$\varepsilon_\perp^{BF} = (d_{31} + \nu d_{33})E. \quad (7)$$

The Young's modulus Y can then be obtained from the value of the blocking stress σ^{BF} (4) required to cancel the longitudinal piezoelectric strain, and the Poisson's ratio ν can be obtained from the corresponding transverse strain $\varepsilon_\perp^{BF}$ (7)

$$\begin{cases} Y = \dfrac{-\sigma^{BF}}{d_{33}E} \\ \nu = \dfrac{\varepsilon_\perp^{BF} - d_{31}E}{d_{33}E}. \end{cases} \quad (8)$$

When the blocking stress σ^{BF} is reached, a residual strain $(\varepsilon = (d_{31} + \nu d_{33})E)$ remains in the transverse direction - unless the material properties satisfy $d_{31} = -\nu d_{33}$, in which case the transverse strain is zero.

From the simple macroscopic analysis of the blocking force test shown in Fig. 1, a procedure to estimate elastic and piezoelectric parameters can be proposed—as shown in Sec. IV A. It is clear that the application of a uniaxial compressive stress can suppress the longitudinal piezoelectric strain but that the macro-strain tensor is not reduced to zero. This was expected since electric field and stress influence the ferroelectric material differently at the microscopic scale. From these results, it is interesting to investigate if a local analysis of the blocking force test could allow estimating single crystal parameters from a test performed on a polycrystal. This is the object of Secs. III–IV.

III. SYNCHROTRON XRD EXPERIMENTS

The experiments were performed on a $Pb_{0.98}Ba_{0.01}$ $(Zr_{0.51}Ti_{0.49})_{0.98}Nb_{0.02}O_3$ (PZT 51–49) ceramic. The processing details have been previously described elsewhere.[14,17] The mean Feret's diameter of the grain size ($d_F \pm$ std. dev.) and relative density, determined by the Archimedes method, were found to be $4.1 \pm 1.9\,\mu m$ and 96.6%, respectively. The material was sectioned and ground into bars having a final geometry of $1\,mm \times 1\,mm \times 3\,mm$ for synchrotron measurements. Silver electrodes were sputtered onto opposing $1\,mm \times 3\,mm$ faces for the application of electrical fields.

The x-ray diffraction experiments were performed at the ID11 beamline at the European Synchrotron Radiation

Facility (ESRF, Grenoble, France). The experimental conditions have been described in a previous paper.[14] The beam energy was set to 78.395 keV and the beamsize was $100 \times 100\,\mu m^2$ at the sample position. Only a quadrant of the Debye-Scherrer rings was recorded, as shown in Fig. 2(a). The 2-D images were converted to 1-D diffraction patterns using the Fit2D software package.[18,19] The 2-D image data, which covered just over a quarter of the circular diffraction pattern, were caked into ten 1-D slices with Fit2D, yielding 1-D diffraction patterns covering grain orientations from 0° to 90° (azimuthal orientation ψ).

The experimental rig (Fig. 2(b)) comprises two metallic pieces between which the specimen is placed. A steel ball is used as a ball-and-socket joint to ensure a solely uniaxial compression state in the specimen. The specimen itself is surrounded by oil (Fluorinert ^{TM} FC-70 Electronic Liquid) to prevent arcing during the application of the electric field. An electric field up to 4 kV/mm was applied using a high voltage amplifier (Chevin Research HVA1B). The whole rig was mounted in a compact MTEST Quattro Materials Testing System loading device[20] to apply the stress.
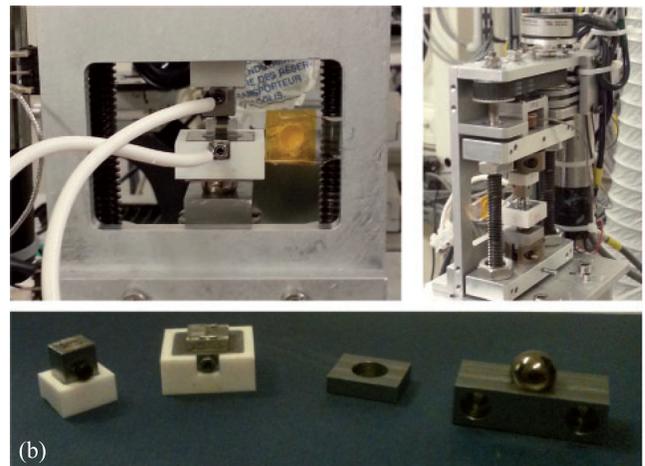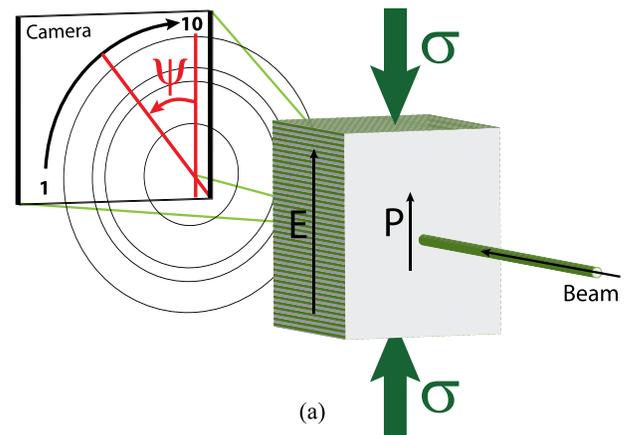
FIG. 2. Measurement setup. (a) Schematic view of the measurement configuration. Electric field and applied stress are parallel. The incident beam is normal to the electric field. The camera is placed so as to capture only a quadrant of the rings in order to increase resolution. The results are divided into ten banks denoted 1–10, corresponding to an azimuthal angle ψ from 90° to 0°. (b) Photos of the measurement setup: parts (bottom), mounted rig (top left), and general view within the electromechanical compression device (top right).
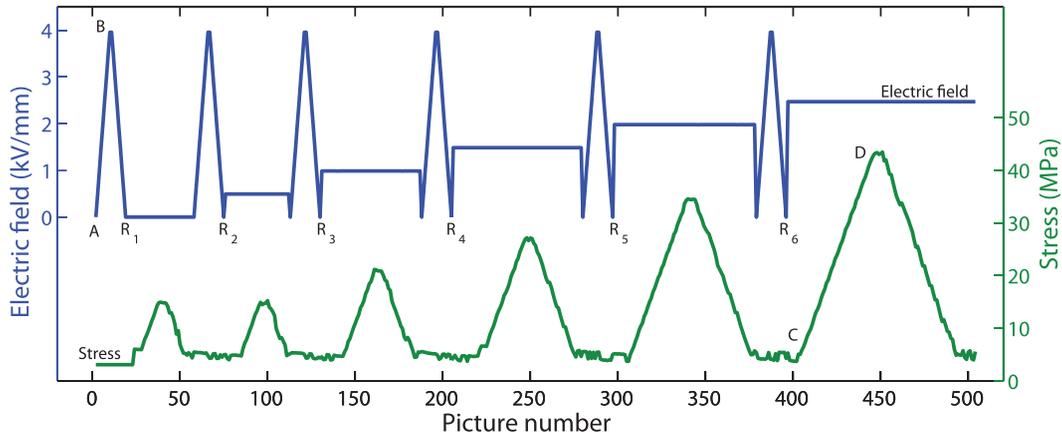
FIG. 3. External electromechanical loading during the *in-situ* experiment: electric field (top) and compressive stress (bottom).

A. Experimental procedure

The experimental procedure was as follows: the sample was first poled, or repoled, under an electric field of 4 kV/mm. With the sample in this poled reference state, a static electric field E was applied, modifying the strain of the material through a combination of the piezoelectric effect and ferroelectric domain switching. A compressive stress was then applied to the material, so as to approximately cancel the longitudinal strain. The value of the maximum stress was estimated from the macroscopic properties of the material (piezoelectric coefficient and Young's modulus), and the experiment was set up so as to go slightly beyond this estimated value. During this process, the lattice spacing d_{hkl} of selected planes was measured *in-situ* by recording XRD patterns at specific loading conditions. Both single and double peak profiles have been fitted using a Matlab procedure based on pseudo-Voigt distribution functions. Upon releasing the stress, a new cycle was initiated for another value of the electric field E. The loading sequence is presented in Fig. 3. In order to maintain contact between the mechanical loading frame and the testing rig, a minimum compression stress of approximately 5 MPa was maintained during the whole procedure. Typical diffraction profiles for the {111} and {200} peaks are given in Appendix A for the first poling and for a compressive stress loading at 2.5 kV/mm.

B. Lattice spacings

The lattice spacings in the initial—unpoled—state were analysed as a function of the azimuthal angle ψ. The obtained values vary in an interval of $\pm 4 \times 10^{-4}$ Å. This interval will be considered in the following as the error bar for the measured lattice spacings. No correlation between the lattice spacing and the azimuthal angle was found, which is consistent with an unpoled state with negligible initial internal stresses. The values for {200}, {111}, and {110} planes are given in

Table I. From the values of d_{002} and d_{200}, the ferroelectric spontaneous strain λ_0 can be estimated approximately to be

$$\lambda_0 = 2 \frac{c - a}{c + 2a} = 2 \frac{d_{002} - d_{200}}{d_{002} + 2 d_{200}} \approx 1.61\%. \quad (9)$$

The evolution of (111), (002), and (200) lattice spacings during the course of the experiment are reported in Appendix B. When considering the peak positions under maximum electric field (4 kV/mm) and in the (re-)poled configuration, a progressive drift of the position is observed. This drift has been fitted separately on the curves for $\psi = 0$ and $\psi = 90°$ by taking as reference the values at maximum field (4 kV/mm) and the values just after repoling. It was found to be very similar on both curves as illustrated by the dashed lines in Fig. 23. This drift is unexplained and could result from a slight drift in the wavelength of the beam during the experiment. Similar drifts are found for the other lattice spacings but are less evident due to the larger variations observed in the lattice spacing. The values of d_{hkl} for all the orientations and all diffracting planes have been corrected for this drift. The correction is approximated as a decreasing exponential function and the maximum correction, for the last picture, is less than 6×10^{-4} Å

$$d_{hkl} = d_{hkl}^{raw} + a \left(1 - \exp(-bN)\right), \quad (10)$$

with N the picture number, $a = 6.2 \times 10^{-4}$ Å and $b = 5 \times 10^{-3}$.

C. Monitoring domain switching

The level of domain switching during the course of the experiment can also be obtained from the experimental results. This is done by comparing the intensity I_{002} of the (002) peak relatively to the intensity I_{200} of the (200) peak. In order to normalise the result with the unpoled initial state (index 0), the multiple of random distribution (mrd) proposed by Jones *et al.*[7] is used (11). The same definition can be used for the {110} peaks (12). In the unpoled state, the

TABLE I. Lattice spacings in the initial unpoled state (point A in Fig. 3).

{200}	{111}	{110}
$d_{200} = 1.9218 \pm 0.0003$ Å $d_{002} = 1.9686 \pm 0.0003$ Å	$d_{111} = 2.2361 \pm 0.0004$ Å	$d_{110} = 2.7176 \pm 0.0003$ Å $d_{101} = 2.7491 \pm 0.0003$ Å
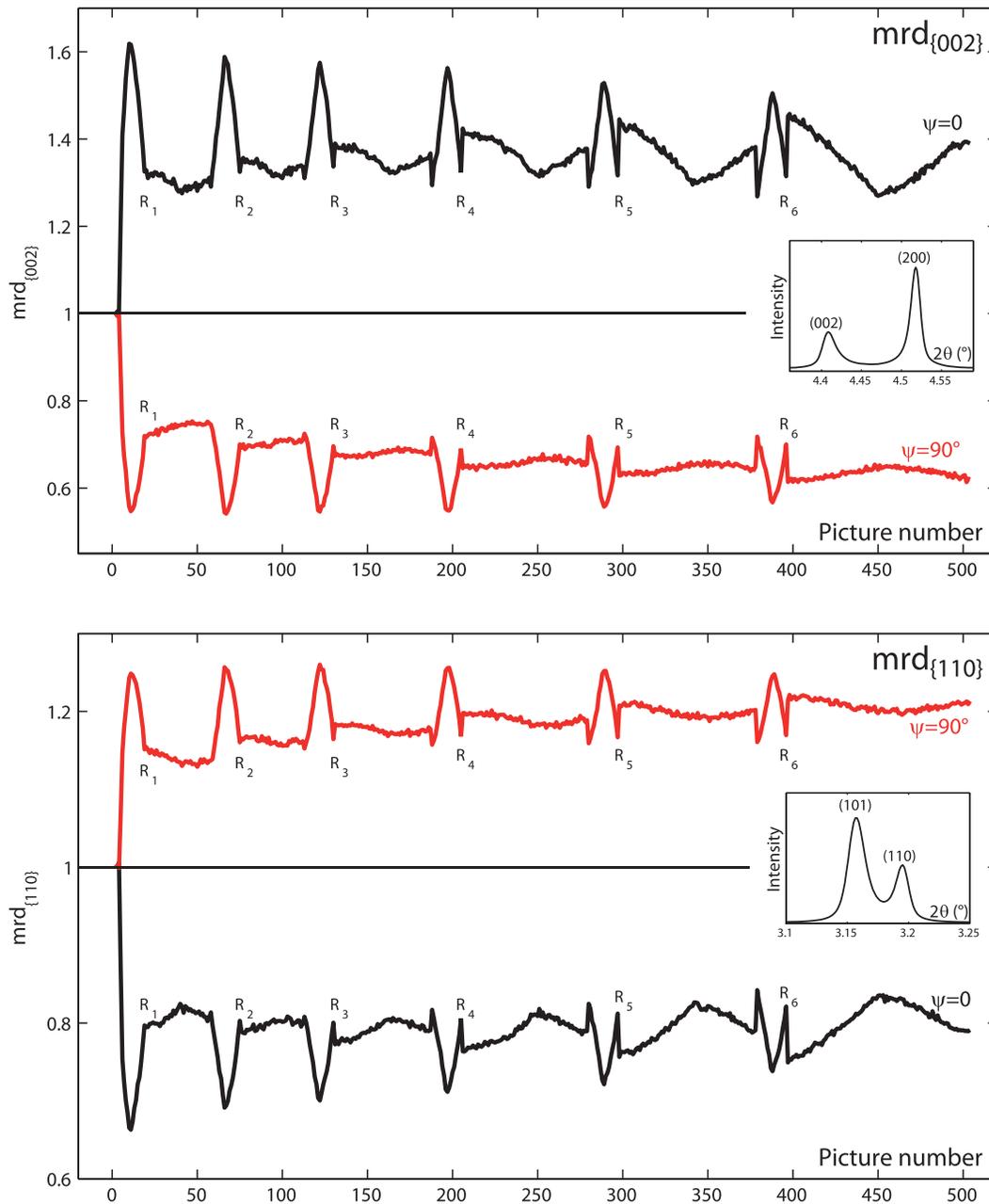
FIG. 4. Evolution of mrd_{002} and mrd_{110} during the *in-situ* experiment, $\psi = 0$ and $\psi = 90°$. mrd_{002} (respectively, mrd_{110}) defines the relative intensities of $\{200\}$ (respectively, $\{110\}$) peaks and quantifies domain switching processes.

mrd values for (002) and (110) are 1, whereas in the fully poled state they are, respectively, 3 and 0

$$mrd_{002} = 3 \, \frac{\dfrac{I_{002}}{I_{002}^0}}{\dfrac{I_{002}}{I_{002}^0} + 2 \dfrac{I_{200}}{I_{200}^0}}, \qquad (11)$$

$$mrd_{110} = 3 \, \frac{\dfrac{I_{110}}{I_{110}^0}}{\dfrac{I_{110}}{I_{110}^0} + 2 \dfrac{I_{101}}{I_{101}^0}}. \qquad (12)$$

The evolution of mrd_{002} and mrd_{110} during the course of the experiment is presented in Fig. 4. As expected the highest amount of domain switching is obtained during the first poling process with a significant increase of mrd_{002} for $\psi = 0$, and a significant decrease for $\psi = 90°$. When the electric field is reduced, the domains switch back so that the mrd_{002} values relax back to relatively low levels at zero field. Subsequent repoling sequences exhibit similar changes in mrd_{002}. When a stress is applied, a decrease of mrd_{002} is observed for $\psi = 0$, particularly at high electric field levels, corresponding to the highest stress level for the blocking force test. This indicates some depoling under stress for this orientation. On the other hand, mrd_{002} was relatively insensitive to the application of stress for $\psi = 90°$ indicating that there was little domain switching for this orientation under stress. The evolution of mrd_{110} follows the same trends, but reversed, with an increase of mrd_{110} for $\psi = 90°$ and a

decrease for $\psi = 0$ when the material is subjected to a poling field. The levels of variation are generally smaller for mrd_{110} compared to mrd_{002}.

D. Lattice strain variations

The data collected can be used to calculate the average strain for a given grain orientation. The strain is calculated from the average lattice spacings $d_{\{hkl\}}$ according to the following equation:

$$\varepsilon_{\{hkl\}} = \frac{d_{\{hkl\}} - d^0_{\{hkl\}}}{d^0_{\{hkl\}}}. \qquad (13)$$

$d_{\{111\}}$ is simply the inter-planar spacing d_{111} for the $\{111\}$ planes as plotted in Appendix B (Fig. 24), while $d_{\{200\}}$ (respectively, $d_{\{110\}}$) is the weighted average of the lattice spacings for the (002) and (200) peaks (respectively, (110) and (101) peaks). Therefore, it should be noted that $d_{\{200\}}$ and $d_{\{110\}}$ incorporate a dependence on the degree of ferroelectric domain switching in addition to the true lattice strain. $d^0_{\{hkl\}}$ is the reference lattice spacing $d_{\{hkl\}}$ in the unpoled state obtained at the beginning of the experiment

$$d_{\{111\}} = d_{111}, \qquad (14)$$

$$d_{\{200\}} = \frac{1}{3}\left(mrd_{002}\, d_{002} + (3 - mrd_{002})\, d_{200}\right), \qquad (15)$$

$$d_{\{110\}} = \frac{1}{3}\left(mrd_{110}\, d_{110} + (3 - mrd_{110})\, d_{101}\right). \qquad (16)$$

The calculated strains are plotted for the $\{200\}$, $\{111\}$, and $\{110\}$ orientations in Fig. 5. All three figures show the same trends, but with different amplitudes. The changes in strain as a function of the frame number correlate well with the variations in applied electric field and compressive stress, plotted in Fig. 3. For $\psi = 0$, the initial positive excursion between frames 0 and 30 corresponds to the first electrical poling procedure, while the subsequent negative excursion between frames 20 and 60 corresponds to the application of the first compressive stress cycle. As the experiment progressed, the starting point for each stress cycle gradually shifted upwards as a result of the increasing static electric field, and the negative excursions grew in magnitude due to the gradual application of higher ultimate stress levels. For $\psi = 90°$, the changes in strain were similar to those described above but opposite in sign. This is expected since the sign of the lateral strains is generally opposite to those of the longitudinal strains. The amplitude of strain strongly depends on the crystallographic orientation. The strain for the $\{200\}$ orientation is the highest, more than three times the strain for the $\{111\}$ orientation. During the application of electric field, it is found that longitudinal and transverse strains are almost identical for $\{111\}$ orientations. It is not the case for the other orientations for which the longitudinal strain is higher in amplitude than the transverse strain. This is a consequence of the distribution of internal stresses and their configuration for different crystallographic orientations. It is also noticeable that the application of stress has little effect on the transverse strain ($\psi = 90°$), whatever the considered orientation.

This could be partially due to the aspect ratio of the samples, which can induce some clamping stresses limiting the lateral expansion of the sample. According to the macroscopic interpretation of the blocking force test, this would indicate a small value for the Poisson's ratio.

E. Local blocking stress curves

The results can also be plotted in terms of blocking stress curves. The strain is then calculated from the lattice spacings $d_{\{hkl\}}$ with reference to the poled state (17) so as to compare with the macroscopic analysis of the blocking force test

$$\varepsilon^{BF}_{\{hkl\}} = \frac{d_{\{hkl\}} - d^i_{\{hkl\}}}{d^i_{\{hkl\}}}, \qquad (17)$$

where $d^i_{\{hkl\}}$ is the reference lattice spacing at the beginning of the blocking force test, just after (re-)poling of the sample (points R_1–R_5 in Fig. 3). The results are shown in Fig. 6 for $\psi = 0$.

For a given applied electric field, the stress-strain curves are approximately linear. The corresponding fitted lines are shown in Fig. 6. To a first approximation, the slopes of the lines can be considered independent of the electric field level. These results are consistent with the macroscopic analysis of blocking stress curves (Sec. II). From these curves, the local blocking stress can be extracted for different levels of electric field. The results are reported in Table II. Here, the local blocking stress is defined as the amplitude of the macroscopic compressive stress for which the local longitudinal strain is cancelled. It does not correspond to the local stress, which can be multiaxial and different from the applied stress due to the material heterogeneity.

The value of the local blocking stress is non-uniform depending on the grain orientation. For a given level of electric field, differences up to 18% can be observed depending on which grain family is considered. For orientations with a $\langle 111 \rangle$ direction parallel to the applied stress, the blocking stress is lower than for orientations with a $\langle 200 \rangle$ direction parallel to the applied stress. This indicates that even if the macroscopic blocking stress cancels the macroscopic longitudinal strain, it does not cancel locally the longitudinal strain. The level of remanent longitudinal strain, which is zero only on average, depends on the crystallographic orientation. In the case of this tetragonal material, the $\langle 111 \rangle$ directions are elastically stiffer than the $\langle 100 \rangle$ directions so that the slope of the blocking stress curves is steeper for $\{111\}$ compared to $\{100\}$ (if, according to the standard interpretation of the blocking force test, the role of domain switching is neglected during the compressive load). The strains due to the electric field (due to the piezoelectric effect—according to the standard interpretation—but possibly incorporating also domain switching), however, are larger along the $\langle 100 \rangle$ directions. These two features act in opposition and tend to homogenise the blocking stress value between $\{111\}$ and $\{100\}$. In the case of a rhombohedral material for which $\langle 111 \rangle$ electric field induced strains are larger than $\langle 100 \rangle$, the two effects would combine to increase the heterogeneity of the blocking stress as a function of the crystallographic orientation.
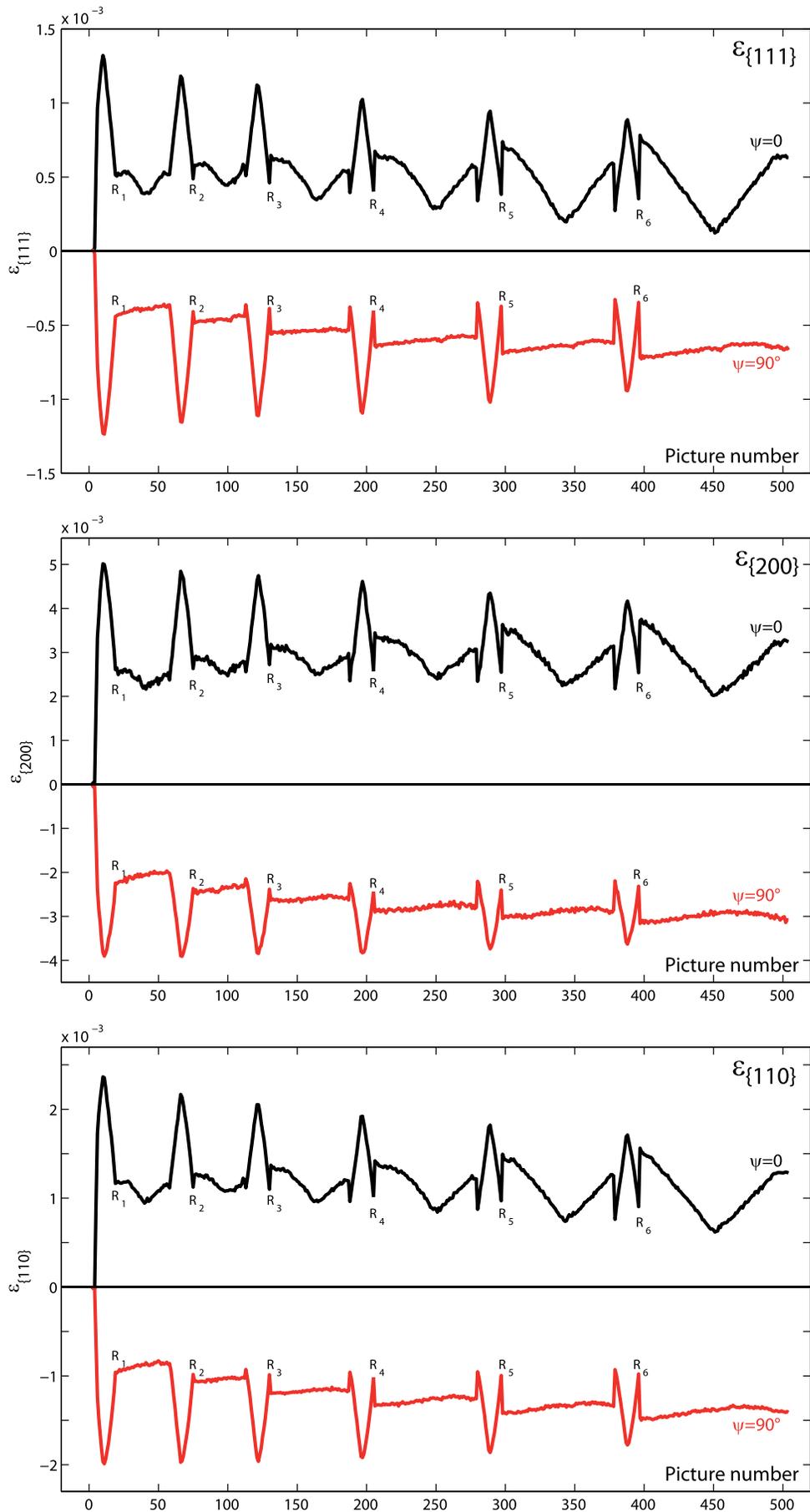
FIG. 5. Evolution of $\varepsilon_{\{111\}}$, $\varepsilon_{\{200\}}$, and $\varepsilon_{\{110\}}$ during the *in-situ* experiment, $\psi = 0$ (top) and $\psi = 90°$ (bottom).
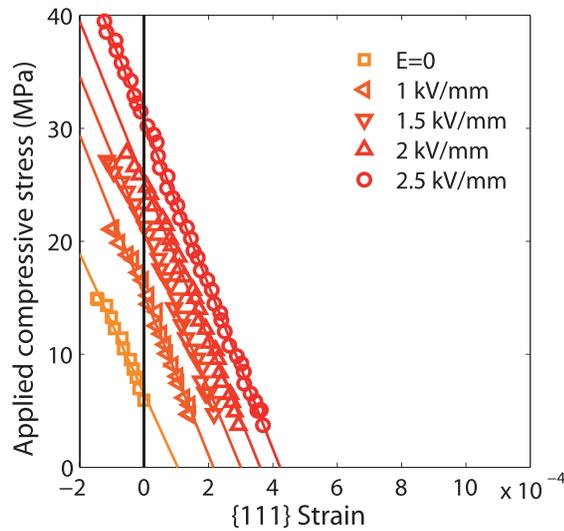
(a) {111} blocking stress curves
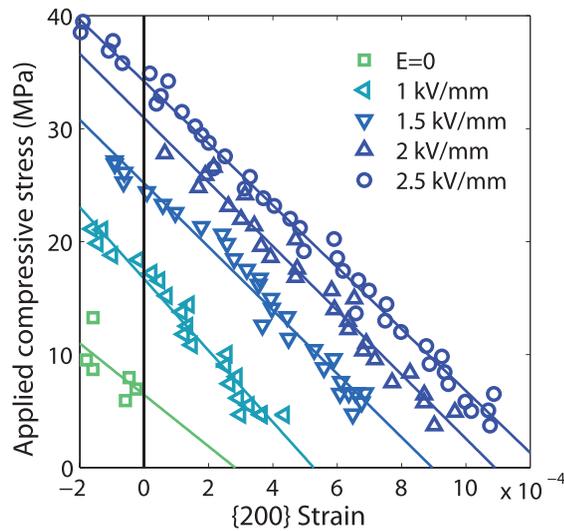
(b) {200} blocking stress curves
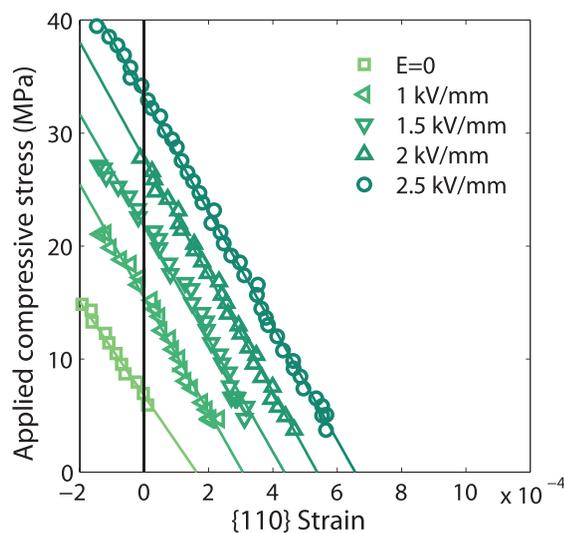
(c) {110} blocking stress curves

FIG. 6. Analysis of diffraction profiles: blocking stress curves obtained for $\psi = 0$ at several levels of applied electric field. Experimental measurements (markers) and corresponding linear fitting (lines). (a) {111} blocking stress curves, (b) {200} blocking stress curves, and (c) {110} blocking stress curves.

TABLE II. Value of the local blocking stress as a function of the grain orientation for different levels of electric field. The error bars give the standard deviation ($\pm$std) obtained on the blocking stress value from the uncertainty on the linear fitting of the data in Fig. 6.

		Plane perpendicular to the applied stress		
		{111}	{200}	{110}
Electric	1.0 kV/mm	15.2 ± 0.7 MPa	16.7 ± 1.3 MPa	15.9 ± 0.7 MPa
field	1.5 kV/mm	20.7 ± 0.8 MPa	25.2 ± 1.3 MPa	21.7 ± 1.0 MPa
	2.0 kV/mm	25.4 ± 0.7 MPa	31.0 ± 1.4 MPa	28.6 ± 0.7 MPa
	2.5 kV/mm	30.6 ± 0.5 MPa	34.2 ± 1.0 MPa	33.1 ± 0.6 MPa

The blocking stress curves also show a dependence on the azimuthal angle ψ, as illustrated in Fig. 7 for an electric field of 2.5 kV/mm. As expected, for orientations approximately aligned with the mechanical loading and electric field axis ($\psi = 0$), the strain decreases with the application of compressive stress while it increases for orientations close to 90°. Again it is evident that the macroscopic stress cancelling the local longitudinal strain is non-uniform within the material. It is also noteworthy that even if the local longitudinal strain is cancelled by the macroscopic stress, the other components of the strain are not. For example, on Fig. 7(a), a macroscopic stress of −31 MPa cancels the longitudinal strain ($\psi = 0$) but leaves the transverse strain $\psi = 90°$ almost unchanged. Although the intersection of the curve for $\psi = 90°$ with the vertical axis cannot be determined accurately it is clear that a very high level of compressive stress would be required to cancel the transverse strain. The same conclusions can be drawn from Figs. 7(b) and 7(c). A notable conclusion is that, contrary to the standard interpretation of the blocking force test in which the compressive stress is supposed to cancel the effects of the applied electric field, the initial state before application of the electric field cannot be fully recovered by the application of a compressive stress. More generally, this highlights the fundamental difference in the nature of the stress (second order tensor field) and the electric field (vector field), which implies that the application of stress cannot cancel the local changes in the domain structure induced by the application of an electric field.

It is also interesting to monitor the azimuthal strain corresponding to the blocking force test, as schematically shown in Fig. 1(b) for the macroscopic measurement. In order to put an emphasis on the initial state of the material, in this case, the strain is calculated with reference to the unpoled state (13). The results are shown in Fig. 8.

The presence of an initial heterogeneous strain in the poled state even in the absence of external loading is evident from Fig. 8. Compared to the unpoled state, the material is elongated along $\psi = 0$ and shortened along $\psi = 90°$ as is expected after the poling process. The elongation and shortening are higher in amplitude for the {200} orientation, which experiences the highest level of domain switching. The smallest strains are obtained for {111} orientations. For this particular orientation, the strain is not directly sensitive to domain switching, so that the measured values are due solely to internal stresses and the intrinsic piezoelectric effect. Fig. 8 then indicates a tensile residual stress along $\psi = 0$ for {111}
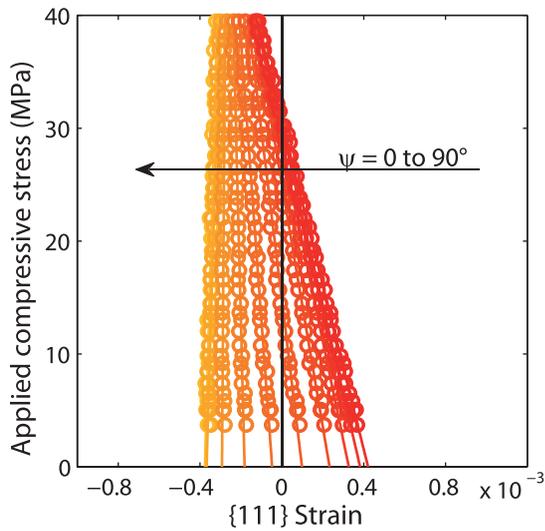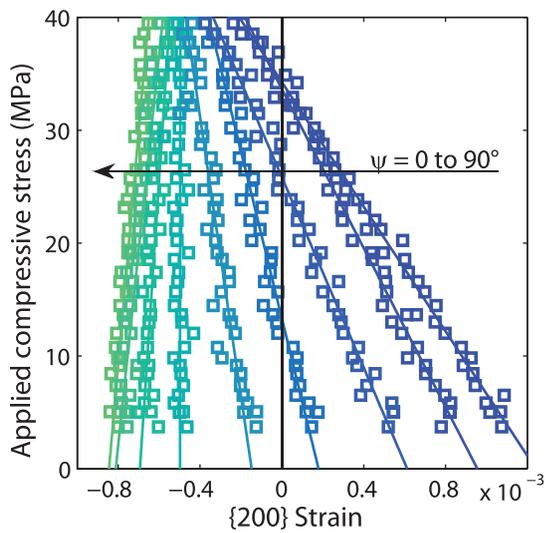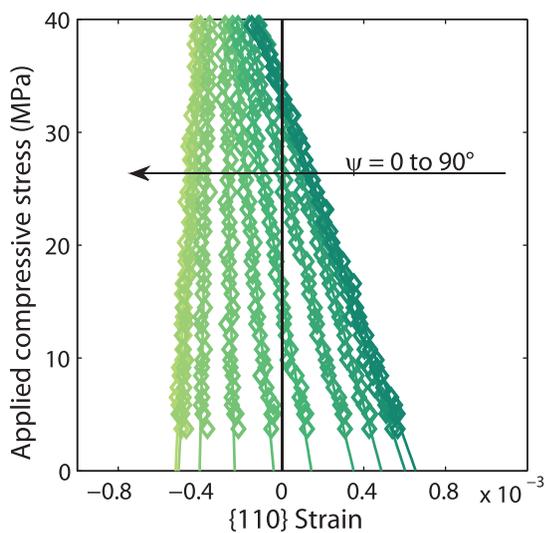
FIG. 7. Analysis of diffraction profiles: blocking stress curves obtained for $\psi = 0°$–$90°$ $(10°$ steps) for an applied electric field of 2.5 kV/mm. Experimental measurements (markers) and corresponding linear fitting (lines). (a) {111} blocking stress curves, (b) {200} blocking stress curves, and (c) {110} blocking stress curves.
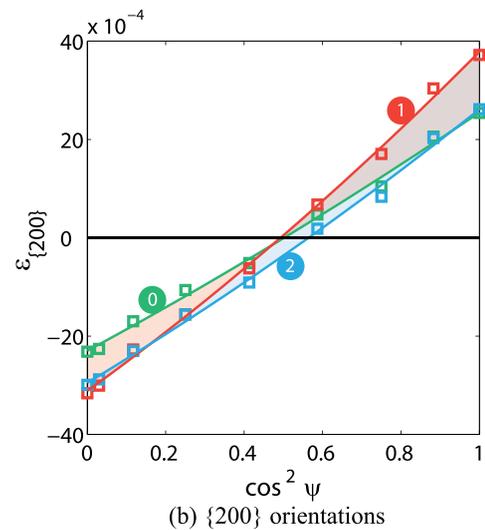
FIG. 8. Evolution of the {111}, {200}, and {110} local strains as a function of the azimuthal angle ψ. Note that in this case the strain is calculated with reference to the unpoled state. Stage ⓪ is the poled configuration under no applied loading. An electric field of 2.5 kV/mm (along $\psi = 0$) is applied at stage ①. A compressive stress (along $\psi = 0$) is then applied at stage ② while maintaining the electric field constant. The magnitude of stress required to cancel the macroscopic strain is approximately 34 MPa. The lines are obtained from a second order polynomial fit and are just plotted to guide the eye. (a) {111} orientations, (b) {200} orientations, and (c) {110} orientations.

(a) Blocking stress curve

(b) Azimuthal strain
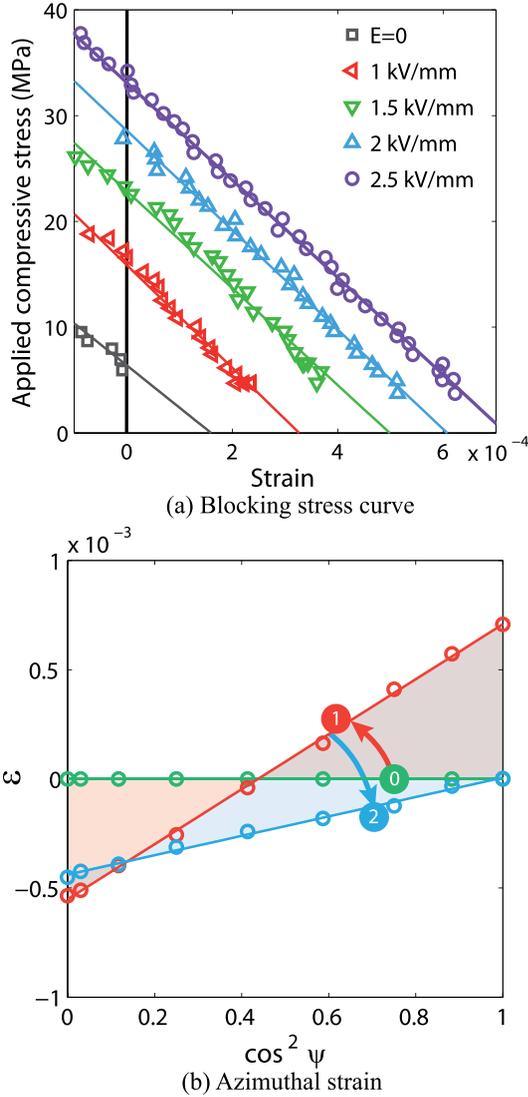
FIG. 9. Reconstruction of the macroscopic blocking force test results from the weighting of the {111}, {200}, and {110} peak contributions: calculated values (dots) and corresponding linear fitting (lines). The strain is calculated with reference to the poled state. (a) Blocking stress curves: at different levels of electric field; (b) azimuthal strain: evolution of the strain as a function of the azimuthal angle ψ. Stage ⓪ is the poled configuration under no applied loading. An electric field of 2.5 kV/mm (along $\psi = 0$) is applied at stage ①. A compressive stress (along $\psi = 0$) is then applied at stage ② while maintaining the electric field constant. The magnitude of stress required to cancel the macroscopic longitudinal strain is approximately 34 MPa.

orientations. For {200} and {110} orientations, the measured strains are a weighted average from two different peaks and thus incorporate all the deformation mechanisms including domain switching. When the static electric field is applied, the curves drift to higher strain values for $\psi = 0$ and to lower strain values for $\psi = 90°$, pushing the material towards a higher polarisation state. According to the linear analysis of the blocking force test, we would expect the curves to intersect on the horizontal axis. It is not exactly the case here. The correction of the drift explained in Sec. III B may not be accurate enough to ensure this property. When the compressive stress is applied, the longitudinal strain is approximately cancelled for all the orientations, but as already mentioned the other components of the strain tensor are not cancelled. It is noticeable, as already observed above, that the transverse strain is hardly modified by

TABLE III. Values of the measured and reconstructed macroscopic blocking stress for different levels of electric field.

Electric field level (kV/mm)	1.0	1.5	2.0	2.5
Measured blocking stress (MPa)	22	33	44	56
Reconstructed blocking stress (MPa)	16	23	29	33

the application of stress, indicating a very low apparent Poisson's ratio. The lines drawn on the figure have been obtained from a second order polynomial fitting and are just a guide for the eyes. A linear dependence of the strain as a function of $\cos^2 \psi$ is often assumed.[5] It is worth noting that this expected dependence is based on the assumption of no initial internal stresses and isotropic elasticity,[21] which is not guaranteed at all for piezoelectric ceramics.[14]

F. Reconstruction of macroscopic blocking stress curves

In principle, the knowledge of local strains allows an estimation of the macroscopic strain $\bar{\varepsilon}$ based on volume averaging ($\bar{\varepsilon} = \langle \varepsilon \rangle$). However, this knowledge of the local strain is here very fragmented and limited to a few orientations only. It is, however, possible to reconstruct some information on the macroscopic strain based on a weighting of peak contributions[22,23]

$$\bar{\varepsilon}(\psi) = \frac{\sum\limits_{hkl} T_{hkl}\, m_{hkl}\, \varepsilon_{\{hkl\}}(\psi)}{\sum\limits_{hkl} T_{hkl}\, m_{hkl}}. \tag{18}$$

$\bar{\varepsilon}(\psi)$ is the component of the macroscopic strain tensor projected along the direction ψ, $\varepsilon_{\{hkl\}}(\psi)$ is the local strain along the direction ψ for the orientation $\{hkl\}$, T_{hkl} is the texture index, and m_{hkl} is the multiplicity of the reflection for $\{hkl\}$ planes. This expression relies on very strong assumptions and notably isotropic elasticity at the local scale, so that it is expected to give only indicative values. Treating the material as cubic and considering no crystallographic texture, T_{hkl} reduces to 1 for any hkl, and m_{hkl} is 8, 6, and 12 for {111}, {200}, and {110} orientation, respectively. The reconstructed macroscopic results for the blocking stress curves and for the azimuthal strain are given in Fig. 9. The strain has been calculated here with reference to the poled state so as to comply with the macroscopic interpretation of the blocking force test (Fig. 1).

The blocking stress curves are approximately parallel lines (Fig. 9(a)), in agreement with the macroscopic interpretation of the blocking force test. The values obtained for the blocking stress at different electric field levels are significantly lower than those obtained independently from macroscopic measurements (see Table III). The approximations made in the reconstruction of the macroscopic strain cannot explain this discrepancy. The macroscopic measurements have been performed on the same material but with a different geometry, which could in part explain the difference. As mentioned earlier, the aspect ratio of the samples for the synchrotron experiment may induce some clamping stresses, modifying the stress distribution in the sample, and then the blocking stress.

TABLE IV. Values of the apparent piezoelectric and elastic macroscopic coefficients identified from the macroscopic interpretation of the blocking force test.

		Electric field level (kV/mm)	1.0	1.5	2.0	2.5
Piezoelectric coefficients	d_{33} (pm/V)		280	310	290	280
	d_{31} (pm/V)		−210	−220	−230	−220
Elastic coefficients	Poisson's ratio ν		0.05	0.11	0.17	0.16
	Young's modulus Y (GPa)		57	50	50	47

The polarisation procedure may also have been different so that the poled state is not the same in two experiments.

Concerning the azimuthal strain (Fig. 9(b)), the poled state ⓪ defines the zero strain and gives the horizontal line as the starting point for the strain. When the electric field is applied ①, the strain is positive in the longitudinal direction and negative in the transverse direction. The longitudinal strain is then cancelled by application of the blocking stress ②, and we note again that the transverse strain is almost unchanged after application of the stress. It is noticeable that the linear fit of $\bar{\varepsilon}(\psi)$ with respect to $\cos^2\psi$ is very satisfying on this macroscopic curve.

This section has presented high energy x-ray diffraction measurements performed *in-situ* during a blocking force test. Domain switching and average strain have been monitored for {111}, {200}, and {110} orientations. Local blocking stress curves have been obtained and an approximation of the macroscopic blocking stress curves was reconstructed using an averaging operation. Both local and macroscopic (reconstructed) results showed a satisfying linearity and are consistent with the standard interpretation of the blocking force test presented in Sec. II. An identification of macroscopic and local properties for the piezoelectric ceramic can then be attempted. This is the objective of the Sec. IV A.

IV. DISCUSSION ON THE INTERPRETATION OF THE BLOCKING FORCE TEST

A. Linear interpretation

From the results of Fig. 9(b), plotted for all levels of tested electric field, macroscopic material parameters can be deduced according to the linear interpretation of the blocking force test presented in Sec. II (see Fig. 1). The validity of this linearity assumption, allowing a simple determination of apparent material parameters, will be discussed in Sec. IV B. The obtained values are summarised in Table IV. The piezoelectric coefficients d_{33} and d_{31} are obtained from the values of the fitted line at stage ① for $\cos^2\psi = 1$ and $\cos^2\psi = 0$, respectively. The Poisson coefficient is obtained from the value of $\cos^2\psi$ at the intersection between the fitted lines for stage ① and ② ($\nu = \cos^2\psi_o/(1 - \cos^2\psi_o)$). The Young's modulus is obtained by dividing the reconstructed blocking stress (Table III) by the value of the fitted line for stage ① at $\cos^2\psi = 1$.

The values obtained for the piezoelectric coefficients d_{33} and d_{31} are fairly constant with electric field (variations lower than 10%) and are consistent with the expected values for this kind of material.[24] The values obtained for the Poisson's ratio are rather small. This is consistent with the

observation of very limited change in transverse strain during the application of stress, likely due to a clamping effect preventing free lateral strain. The Poisson's ratio is a parameter very sensitive to perturbations so that it is not surprising to find a big variation as a function of electric field. Concerning the Young's modulus, the identified value tends to decrease with the applied electric field with significant variations. The order of magnitude of the Young's modulus seems reasonable and consistent with published data.[25,26]

Following the same principle, apparent local material parameters can be identified. To be rigorously performed, however, this approach would need an appropriate micromechanical approach in order to define the electric field and
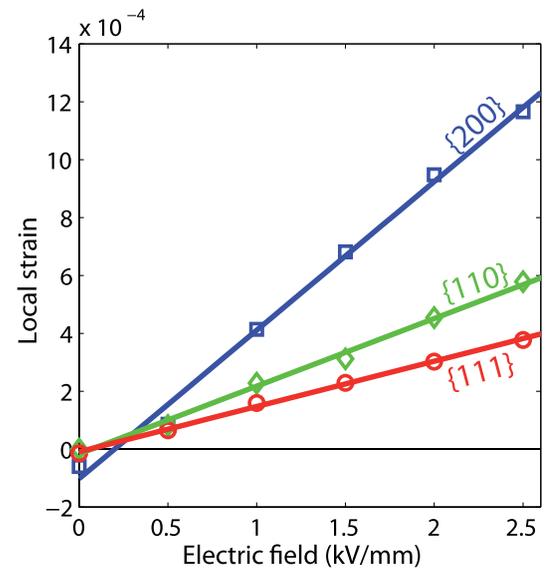
(a) Longitudinal strain (elongation)
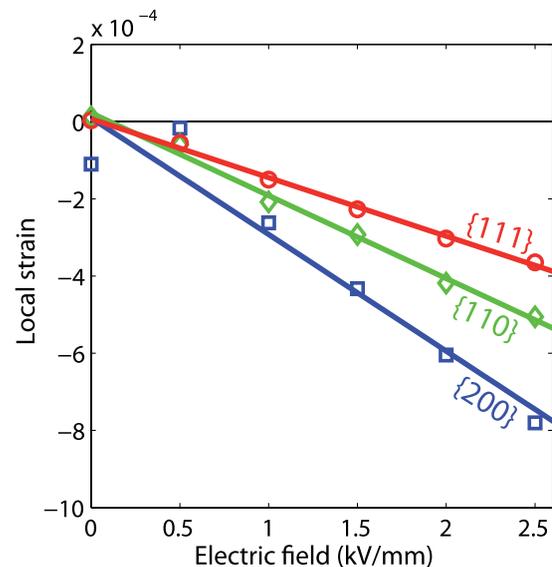
(b) Transverse strain (contraction)

FIG. 10. Apparent longitudinal and transverse strain for several crystallographic orientations obtained from the lattice spacings measured after repoling of the material and application of a constant electric field E during the blocking force test. The strains are calculated with reference to the (re-)poled state. The linear fitting of the curves allows the identification of the apparent longitudinal and transverse piezoelectric coefficients. (a) Longitudinal strain (elongation) and (b) transverse strain (contraction).

TABLE V. Apparent longitudinal and transverse piezoelectric coefficients for directions $\langle 111 \rangle$, $\langle 100 \rangle$, and $\langle 110 \rangle$ from the *in-situ* blocking force test. The error bars give the standard deviation ($\pm$std) obtained from the uncertainty on the linear fitting of the data in Fig. 10.

Electric field orientation (pm/V)	$\langle 100 \rangle$	$\langle 110 \rangle$	$\langle 111 \rangle$
Longitudinal coefficient d_l	513 ± 43	234 ± 18	156 ± 18
Transverse coefficient d_t	-302 ± 89	-214 ± 17	-152 ± 10

stress in a given crystallographic orientation. Indeed, material heterogeneity, local anisotropy, microstructure topology, and material defects are a source of intra- and inter-granular heterogeneity for the electromechanical loadings. Such a micro-mechanical approach, limited to intergranular heterogeneities, has been proposed recently[27] and has been applied to the case of the piezoelectric blocking force test to account for stress heterogeneity within the material.[14] In this paper, the analysis will be performed assuming uniform stress and electric field within the material, as the single crystal material parameters are unknown. The results are then to be considered more from a qualitative point of view.

The local piezoelectric behaviour is analysed by studying the local strain of the (re-)poled material under constant electric field (with no applied stress). For each level of tested electric field, the strain can be extracted for {111}, {200}, and {110} planes. The strain is calculated with reference to the poled state so as to evaluate an apparent piezoelectric behaviour. The data for $\psi = 0$ provide an apparent longitudinal piezoelectric coefficient, while the data for $\psi = 90°$ provide an apparent transverse piezoelectric coefficient. The results are plotted in Fig. 10.

Despite a discrepancy for the transverse coefficient at 0.5 kV/mm, the linear fitting of the curves gives a reasonable approximation of the apparent piezoelectric coefficients for each crystallographic direction. The corresponding estimates are given in Table V. The uncertainty on these values, obtained from the analysis of the fitting procedure, is relatively high, particularly for the $\langle 100 \rangle$ direction, most affected by the measurement at 0.5 kV/mm.

The relationship between the apparent piezoelectric coefficient and the single crystal properties is not trivial, since it depends on the level of domain switching reached after the (re-)poling process. If we assume uniform electric field within the material, the direction $\psi = 0$ is the direction of the electric field for any crystallographic orientation. This orientation being known, the longitudinal and transverse

TABLE VI. Apparent longitudinal piezoelectric coefficient expressed as a function of the standard piezoelectric coefficient for the single crystal. The calculation is performed under the assumption of tetragonal symmetry, pure piezoelectric behaviour, uniform electric field within the material, and absence of crystallographic texture.

	d_l
$\langle 100 \rangle$	$\frac{1}{3}\mathrm{mrd}_{002}(\psi = 0)\, d_{33}$
$\langle 110 \rangle$	$\frac{(3 - \mathrm{mrd}_{110}(\psi = 0))}{6\sqrt{2}}(d_{33} + d_{31} + d_{15})$
$\langle 111 \rangle$	$\frac{1}{3\sqrt{3}}(d_{33} + 2d_{31} + 2d_{15})$
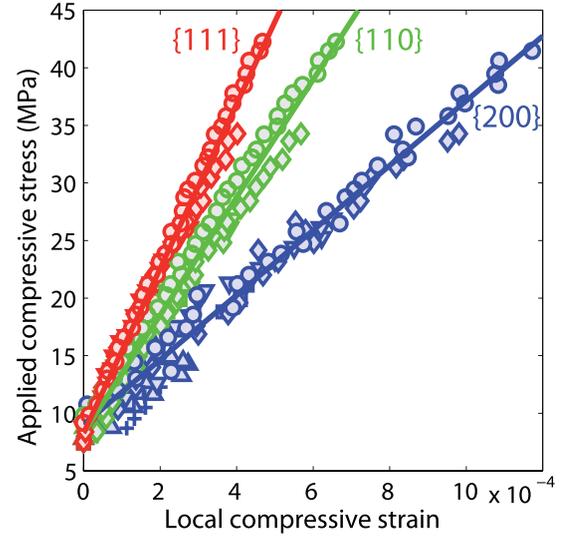
(a) Stress-strain curve for $\psi = 0$
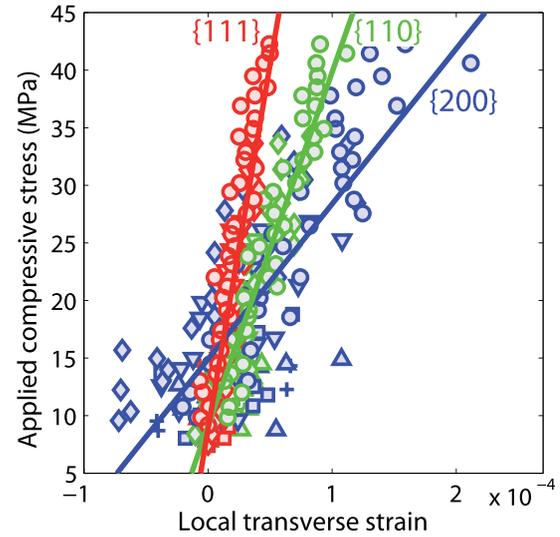
(b) Stress-strain curve for $\psi = 90°$

FIG. 11. Apparent elastic coefficients when applying the compressive stress during the blocking force test. The longitudinal and transverse strains are calculated with reference to the lattice spacing after (re-)poling. The longitudinal strain is obtained from the results at $\psi = 0$, and the transverse strain from the results at $\psi = 90°$. Different markers denote different electric field levels ($\triangle$, $\square$, $\triangledown$, $\diamond$, and $\bigcirc$ denote 0.5, 1, 1.5, 2, and 2.5 kV/mm, respectively). The linear fit for $\langle 111 \rangle$, $\langle 110 \rangle$, and $\langle 100 \rangle$ directions is also plotted. (a) Stress-strain curve for $\psi = 0$ and (b) stress-strain curve for $\psi = 90°$.

piezoelectric strains can be calculated for any orientation (ϕ, θ, α) (see Appendix C, Table IX). Assuming no crystallographic texture, the average longitudinal and transverse strain can be obtained by integrating the relevant expressions over the appropriate orientations. The case of the longitudinal strain can be dealt with easily since its expression is a constant for a given set of orientations. The apparent piezoelectric coefficients are then the ratio between the longitudinal strain and the electric field amplitude.

For a family of directions $\langle hkl \rangle$, the apparent piezoelectric coefficient is the weighted average of all the apparent piezoelectric coefficients for the directions [hkl]. In the case of $\langle 100 \rangle$, $\langle 110 \rangle$, and $\langle 111 \rangle$ directions, the apparent

TABLE VII. Apparent longitudinal and perpendicular moduli Y and $Y_\perp$ for different crystallographic orientations. Numerical values obtained from the *in-situ* blocking force test and theoretical values expressed as a function of the standard compliance tensor for the single crystal. The calculation is performed under the assumption of cubic symmetry, pure elastic behaviour, uniform stress within the material, and absence of crystallographic texture. The error bars give the standard deviation ($\pm$std) obtained from the uncertainty on the linear fitting of the data in Fig. 11.

	Y^a (GPa)	Y^{th}	$Y_\perp^a$	$Y_\perp^{th}$ (GPa)
$\langle 100 \rangle$	28.1 ± 2.4	$\dfrac{1}{S_{11}}$	134.8 ± 5.1	$\dfrac{-1}{S_{12}}$
$\langle 110 \rangle$	51.1 ± 4.4	$\dfrac{4}{2S_{11} + 2S_{12} + S_{44}}$	307.2 ± 2.3	$\dfrac{-8}{2S_{11} + 6S_{12} - S_{44}}$
$\langle 111 \rangle$	71.4 ± 5.7	$\dfrac{3}{S_{11} + 2S_{12} + S_{44}}$	632.0 ± 1.6	$\dfrac{-6}{2S_{11} + 4S_{12} - S_{44}}$

TABLE VIII. Values of the piezoelectric and elastic coefficients for the single crystal identified from the local interpretation of the *in-situ* blocking force test. The identification has been performed assuming linear behaviour, tetragonal structure for the piezoelectric coefficients, cubic symmetry for the elastic behaviour, uniform stress and electric field within the material, and absence of crystallographic texture.

Piezoelectric coefficients (pm/V)		Elastic coefficients (10^{-12} m^2/N)	
d_{33}	1100	S_{11}	36
$d_{31} + d_{15}$	-190	$2S_{12} + S_{44}$	7

longitudinal piezoelectric coefficients d_l are defined by the expressions given in Table VI.

The local elastic behaviour is analysed by studying the local strain under compressive stress (and constant electric field) during the blocking force test. For each level of tested electric field, the strain is extracted for the {111}, {200}, and {110} planes. The strain is calculated with reference to the poled state so as to comply with the linear interpretation of the blocking force test. The data for $\psi = 0$ provide an apparent Young's modulus. The data for $\psi = 90°$ can also be used. The results are plotted in Fig. 11. The macroscopic stress-local strain curves exhibit a linear behaviour. The result shows a very significant elastic anisotropy at the single crystal scale. Assuming uniform stress (Reuss assumption), these curves can be used to identify the local elastic coefficients. A more refined self-consistent approach was proposed in Daniel *et al.*[14] but is not used here for the sake of simplicity. For the transverse strain (Fig. 11(b)), the result is noisy due to the lower amplitude of the measured strain. The linear fitting of the curves, however, provides an estimate of perpendicular modulus. The values obtained for the longitudinal and transverse apparent moduli are summarised in Table VII. The theoretical values assuming purely elastic behaviour and uniform stress within the material (see Appendix C, Table X) are also reported. They are the ratio between the stress amplitude and the strain. The transverse strain is parametrised by an angle, since the perpendicular direction is not uniquely defined by the orientation perpendicular to the compressive stress. Assuming no crystallographic texture, the perpendicular strain has been averaged over all the possible directions perpendicular to $\psi = 90°$, by integrating over the angle orientations.

From this linear analysis of the *in-situ* blocking force test, the elastic and piezoelectric parameters of the single crystal can in theory be identified from the values reported in Tables V and VII. It is worth noting that d_{31} and d_{15} always appear as $(d_{31} + d_{15})$ in the definition of the apparent longitudinal piezoelectric coefficient so that they cannot be distinguished on the basis of this approach (Table VI). The use of transverse apparent coefficients or experimental results obtained in shear mode would overcome this issue. In a similar way, the elastic coefficients S_{12} and S_{44} are linked as $(2S_{12} + S_{44})$ in the different expressions of the apparent Young's modulus (Table VII).

For the piezoelectric coefficients, d_{33} and $(d_{31} + d_{15})$ have been obtained from an optimisation procedure on the three equations (two unknowns). The values of mrd$_{002}$ and mrd$_{110}$ have been obtained from the measurements (average value in the (re-)poled state). Their values are 1.32 and 0.81, respectively. The results are reported in Table VIII. The high values of the apparent piezoelectric coefficients can be explained by the assumption of linearity: all the observed strain is attributed to the piezoelectric effect, notably neglecting the contribution of domain switching. This point will be discussed in Sec. IV C. For the elastic coefficients, the data from the longitudinal (Young's) modulus have been considered as more reliable—they rely on larger strain measurements—and have been used to define the coefficients S_{11} and $(2S_{12} + S_{44})$ from an optimisation procedure. The values are also given in Table VIII. It is recalled that a very simple micro-mechanical scheme has been used here and that the heterogeneity of stress and electric field should be implemented for a more reliable parameter identification. Guidelines for such a piezoelectric homogenization scheme can be found in Corcolle *et al.*[27,28] Due to the level of uncertainty in the values of the apparent piezoelectric and elastic coefficients (Tables V and VII), the uncertainty on the parameters reported in Table VIII is relatively high (of the order of 100 pm/V for piezoelectric coefficients and 10^{-12} m^2/N for elastic coefficients).

In this section, following the standard interpretation of the blocking force test, macroscopic apparent elastic and piezoelectric coefficients were identified from the reconstruction of macroscopic blocking stress curves. It was shown that a similar procedure can be performed at the grain scale to identify local apparent elastic and piezoelectric coefficients. This analysis is based on the assumption of purely linear and reversible piezoelectric and elastic behaviour. In Sec. IV B, the validity of this assumption is investigated.

B. Non-linearities

The linear interpretation of the blocking force test from a macroscopic and local point of view has allowed the definition of useful material parameters. However, despite the initial appearances, many signs of non-linearities can be found during this experiment that are in contradiction with the assumptions made. We try in this section to analyse them.
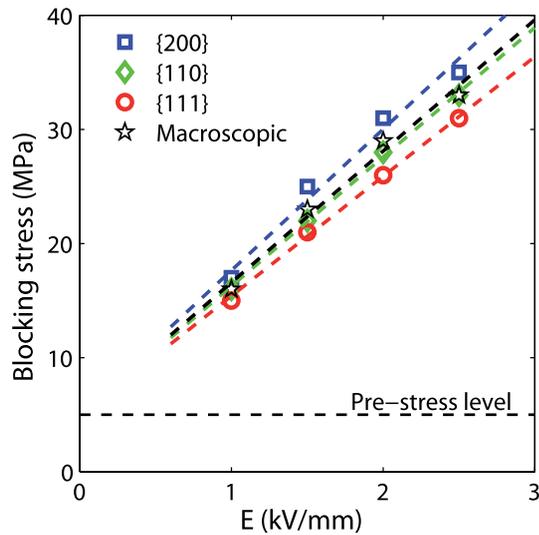
(a) Blocking stress
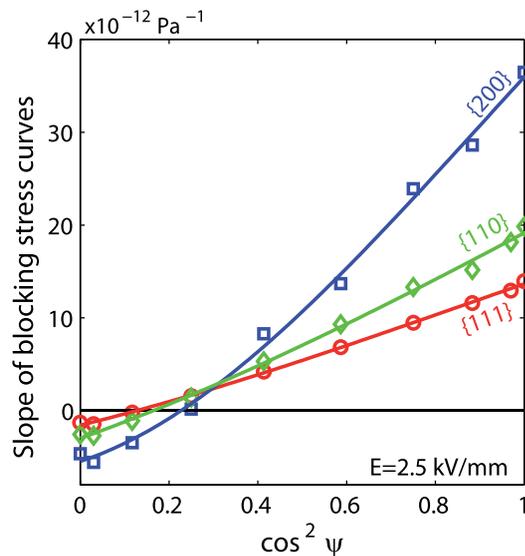
(b) Slope of blocking stress curve

FIG. 12. Signs of non-linear response for the blocking force test. (a) Blocking stress: as a function of the applied electric field, and corresponding linear fitting. The linearity is not precisely verified, particularly for the {200} orientations. (b) Slope of the {200}, {110}, and {111} blocking stress curves: for an applied electric field of 2.5 kV/mm. The line is a second order polynomial used as a guide for the eye. The expected linearity[14] is not verified, particularly the {200} orientations.

A first point is the evolution of the blocking stress with the applied electric field E. A linear dependence is expected, but not observed as shown in Fig. 12(a) for both local and macroscopic blocking stress. Despite the experimental uncertainties, this non-linearity is significant, particularly for the {200} orientations. This suggests again that the application of the compressive stress does not only give rise to elastic behaviour. Another sign of non-linearity is the evolution of the slope of the blocking stress curves as a function of $\cos^2\psi$. Under the assumption of linear elasticity, these slopes are linear functions of $\cos^2\psi$. This property was used by Daniel *et al.*[14] to identify the elastic anisotropy of a rhombohedral PZT single crystal from a polycrystalline sample. Fig. 12(b) shows that this property is not verified here, again particularly for the {200} orientations.
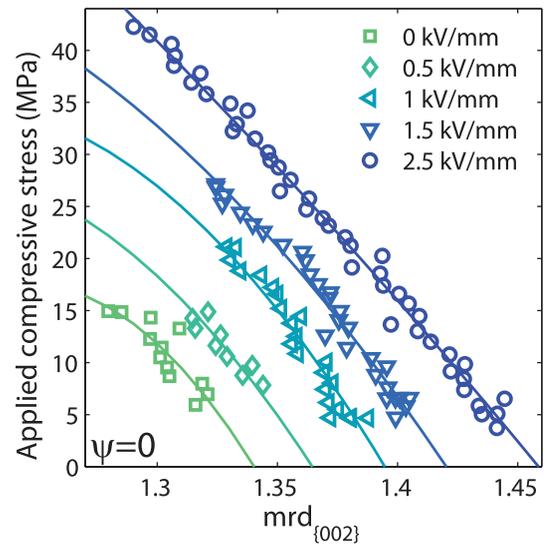
(a) {200} blocking stress curves
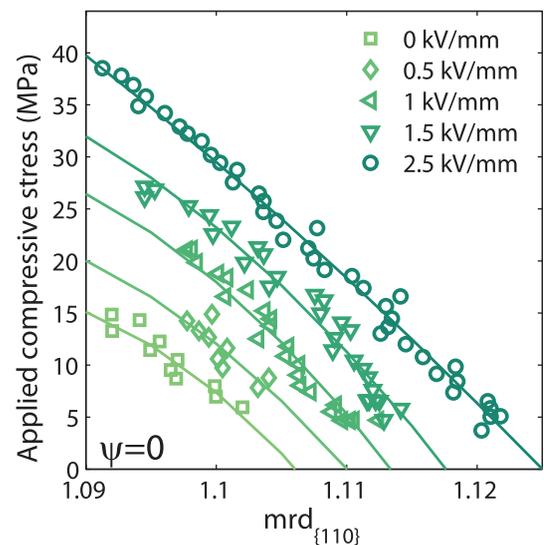
(b) {110} blocking stress curves

FIG. 13. Blocking stress curves showing domain switching during the blocking force test. Results obtained for $\psi = 0$ at several levels of electric field. Experimental measurements (markers) and trend lines to guide the eye. (a) {200} blocking stress curves and (b) {110} blocking stress curves.

C. Role of domain switching

One of the main assumptions for the linear analysis of the blocking force test is the negligible amount of domain switching under electric field and/or stress during the course of the experiment. This amount of domain switching can be monitored during the experiment using the multiple of random distribution mrd_{hkl}. Blocking stress curves can be constructed from the evolution of this parameter instead of the standard blocking stress curves based on the strain estimate. Fig. 13 shows the changes of mrd_{002} and mrd_{110} as a function of the applied compressive stress for different levels of electric field and for $\psi = 0$. The azimuthal analysis of the blocking force test can also be performed for the parameter mrd_{hkl}. Fig. 14 shows the evolution of mrd_{002} and mrd_{110} as a function of the azimuthal angle ψ during a blocking force test. These curves assess the partial depoling of the material during the test.
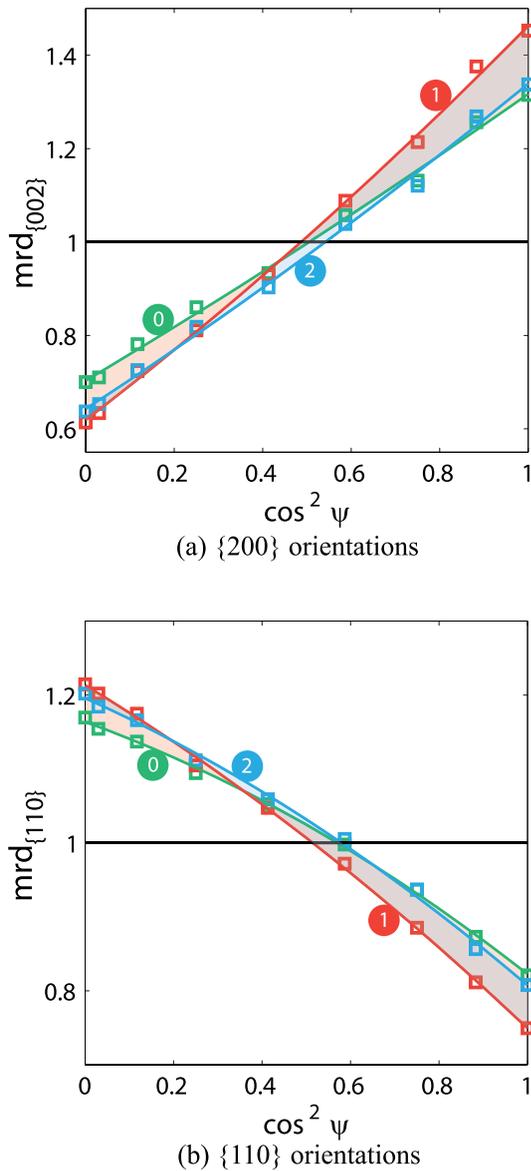
FIG. 14. Evolution of mrd$_{002}$ and mrd$_{110}$ as a function of the azimuthal angle ψ. Stage ⓪ is the poled configuration under no applied loading. An electric field of 2.5 kV/mm (along $\psi = 0$) is applied at stage ①. A compressive stress (along $\psi = 0$) is then applied at stage ② while maintaining the electric field constant. The magnitude of stress is approximately 34 MPa so as to cancel the macroscopic strain. The lines are obtained from a second order polynomial fit and are just plotted for eye guidance. (a) {200} orientations and (b) {110} orientations.

There is clear evidence of domain switching when the material is placed under constant electric field (stage ① Fig. 14). There is also clear evidence of domain switching in the second stage of the blocking force test when the compression stress is applied under static electric field. As expected, the direction of the applied field and stress along $\psi = 0$ is the orientation for which the highest levels of domain switching are observed. These levels, however, are moderate. According to Figure 13(a), for $\psi = 0$, only 5% in volume of the {200} orientations undergo domain switching from the beginning to the end of the compressive stress sequence at 2.5 kV/mm (the variations in mrd$_{002}$ have to be divided by 3 to reflect the volume involved in domain switching). This direction and this crystallographic orientation define the configuration
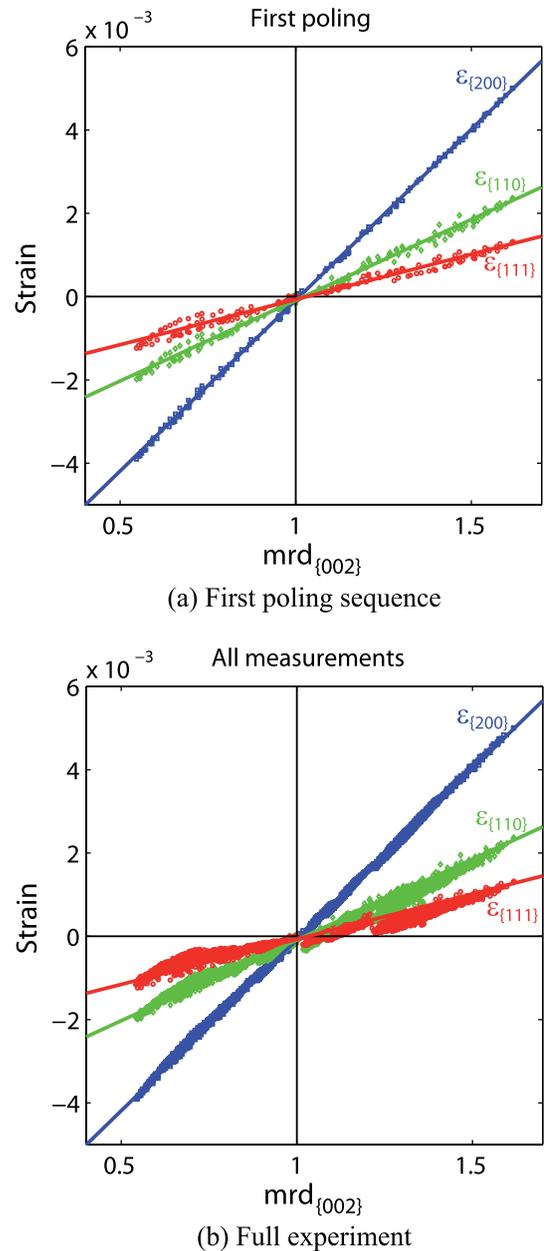
FIG. 15. Correlation between multiple of random distribution mrd$_{002}$ and local strain for different crystallographic orientations. All orientations ψ are regrouped on the figure. (a) First poling sequence and (b) full experiment.

showing the highest levels of domain switching. However, it must be noted that the transformation strain λ_0 (calculated as 1.6% in Sec. III B) is much higher than the levels of elastic strain expected here so that this small volume can contribute significantly to the macroscopic strain.

The domain switching is actually responsible for most of the strain in this material, as shown in Fig. 15.

The relationship between the strain and mrd$_{002}$ during the first poling sequence (points A–R$_1$ in Fig. 3) is plotted in Fig. 15(a). The strain is calculated with reference to the unpoled state and has been plotted for the {200}, {110}, and {111} orientations along all directions ψ (from 0° to 90°). There is a very strong correlation between strain and volume fraction. The slopes of the fitted lines are 8.21×10^{-3}, 3.88×10^{-3}, and 2.17×10^{-3} for {200}, {110}, and {111} orientations, respectively. If we assume that the strain for
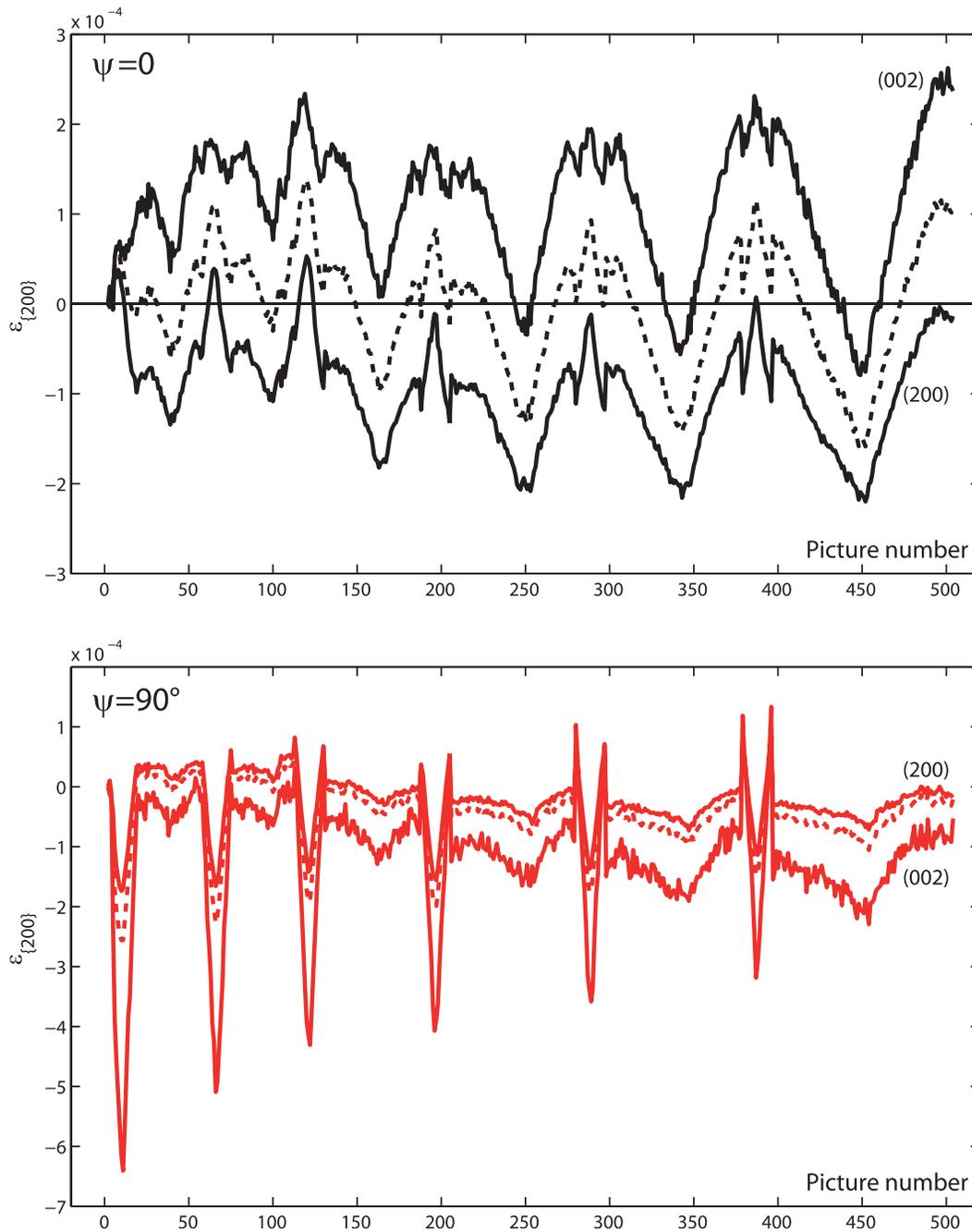
FIG. 16. Evolution of $\varepsilon_{(002)}$ and $\varepsilon_{(200)}$ during the *in-situ* blocking force test for the orientation $\psi = 0°$ (top) and $\psi = 90°$ (bottom). The dotted line is the weighted average of $\varepsilon_{(002)}$ and $\varepsilon_{(200)}$. This graph illustrates the strain for this particular crystallographic orientation without incorporating the transformation strain.

{200} orientations is only due to domain switching, the expected slope would be $\lambda_0/2$ (since a volume fraction $\mathrm{mrd}_{002}/3$ undergoes an expansion λ_0 and a volume fraction $(1 - \mathrm{mrd}_{002}/3)$ undergoes a contraction $\lambda_0/2$ resulting in a total strain of $(\mathrm{mrd}_{002} - 1)\lambda_0/2$). The fitted slope is in surprisingly good accordance with this estimate, suggesting that intrinsic piezoelectricity and elasticity provide a negligible contribution to the strain for this orientation. On the other hand, no ferroelectric strain contribution is expected for {111} orientations. However, the very good correlation between strain and the domain volume fractions, represented by mrd_{hkl}, suggests that the main contribution to the strain

for this orientation is due to the internal stresses resulting from domain switching.

If we now plot the same figure, but include all the data collected during all the poling and loading-unloading cycles together (Fig. 15(b)), the correlation between strain and volume fraction remains very strong and the identified slopes relevant. If the strain was calculated only from these slopes and the knowledge of the multiple of random distribution mrd_{002}, the maximum error would not exceed 2×10^{-4}, 4×10^{-4}, and 4×10^{-4} for $\varepsilon_{\{002\}}$, $\varepsilon_{\{110\}}$, and $\varepsilon_{\{111\}}$, respectively. This suggests that the intrinsic piezoelectric effect and elasticity (associated with the macroscopic compressive
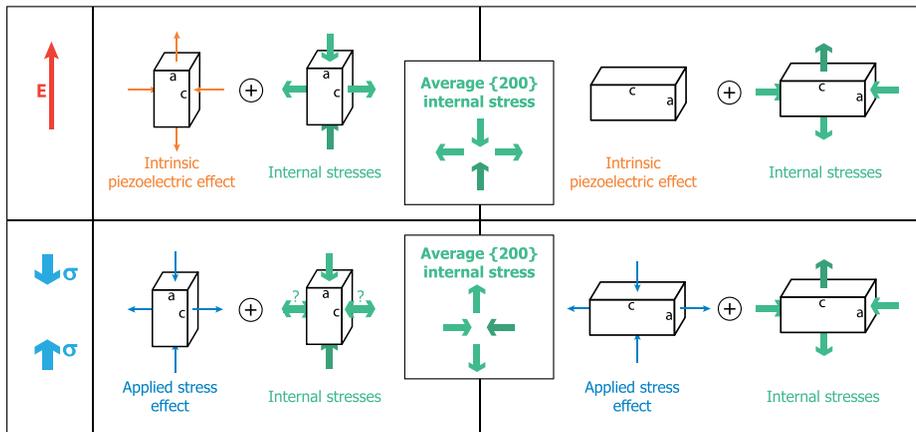
FIG. 17. Schematic view of the effect of an applied load (electric field or stress) for 200 oriented grain as a function of the local polarisation direction. The contributions due to the piezoelectric effect, internal stresses resulting from domain switching and the elastic effect due to the applied stress are separated.

stress) provide a relatively small contribution to the strain compared to the role of domain switching.

In this part, it has been shown that despite the apparent linearity of the blocking stress curves at the local and macroscopic scales, domains switching plays a very significant role in the deformation mechanisms under electric field and stress for this material. For the material studied here, domain switching appears to be the dominant source of local and macroscopic strain, either through transformation strain ({200} orientations) or through internal stresses ({111} orientations).

D. Intragranular strains

The very good agreement between the slope of the line $\varepsilon_{\{002\}}(mrd_{002})$ and the value $\lambda_0/2$ raises some questions on the deformation process for {200} orientations. To analyse this deformation process, the strains for (002) and (200) orientations have been plotted separately. Fig. 16 shows the (002) and (200) strains in the direction $\psi = 0$ and $\psi = 90°$. The analysis can also be conducted from the lattice spacings plotted in Appendix B (Figs. 22 and 23).

The first noticeable feature of these plots is that the strain is of very small amplitude compared to the average strain $\varepsilon_{\{200\}}$ in Fig. 5 (more than ten times smaller). This confirms the dominant role played by domain switching for this orientation. The evolution of the strain during the course of the experiment also gives an insight into the mechanisms at play. During the application of the electric field, if we assume that the local electric field is mainly oriented along the applied electric field direction, an elongation due to the intrinsic piezoelectric effect is expected for $\psi = 0$. However, poling the material also induces compressive residual stress along the poling direction.[5] These two effects seems to be balanced here, resulting in a very small variation of d_{002} under electric field for $\psi = 0$, and hence a very small $\varepsilon_{(002)}$. For $\psi = 90°$, little intrinsic piezoelectric effect is expected on d_{002}, since the corresponding orientation is mostly loaded under shear piezoelectric mode. The residual stress due to domain switching is expected to be tensile along $\psi = 90°$.[5] On the contrary, a significant contraction is observed along this direction. This can be interpreted as an intragranular effect. Due to domain switching, the grain tends to elongate along the poling direction and contract in the direction

perpendicular to the poling. Domains with polarisation along the macroscopic poling direction ($\psi = 0$) are increasing in proportion and contribute to this elongation. They are subjected to the mentioned residual stress. On the other hand, domains with polarisation perpendicular to the macroscopic poling direction ($\psi = 90°$), decreasing in proportion, resist this deformation and are forced into the change of shape of the grain. They are then subjected to a compression along $\psi = 90°$ and to an elongation along $\psi = 0$. This stress is opposite to the average residual stress for the considered orientation and involves a decreasing proportion of the material as the poling process progresses. The observed amplitude for the contraction of d_{002} along $\psi = 90°$ under applied electric field highlights the very high level of intragranular stress heterogeneity depending on the orientation of the polarisation.

When the macroscopic stress is then applied along $\psi = 0$, d_{002} logically decreases for $\psi = 0$. More surprisingly, d_{002} also decreases for $\psi = 90°$ where, due to the Poisson effect, a small expansion would have been expected. The variation is small, within the range of the error bar. This result can also be attributed to the role of internal residual stresses due to reverse domain switching. Domains with polarisation perpendicular to the stress would indeed increase in proportion, contributing to an elongation along $\psi = 90°$, and are then subjected to a compressive stress along this direction in resistance to the change in strain. This local interpretation of the effects of the applied loading as a function of the polarisation direction can be schematically summarised as presented in Fig. 17.

The analysis of the strain $\varepsilon_{(200)}$ is consistent with the proposed scenario. Under an applied electric field, there is an increase of d_{200} for $\psi = 0$ related to the presence of internal stresses as a consequence of domain switching. For $\psi = 90°$, the a-axis is reduced as a result of the competition between intrinsic piezoelectric effect and internal stresses. When the compressive stress is applied, the effect of the applied stress and of internal stresses due to domain switching are opposite for $\psi = 0$. The effect of stress is predominant, leading to a decrease in d_{200}. The a-axis would be expected to increase for $\psi = 90°$ under applied stress, it is actually slightly decreasing, keeping an almost constant value. This would mean that the horizontal component of the internal stresses for this orientation might be compressive. It must be noticed that the variations observed for d_{200} during the experiment are very small

and lie within the range of the error bar. For this orientation, the a-axis could almost be considered as constant.

These results highlight the significant differences in the strains experienced by different domains within a grain. It has been known for a long time that intergranular stresses play a significant role in the behaviour of ferroelectric materials, but the level of intragranular heterogeneity is also very high.

E. Irreversibilities

Another noticeable aspect of the non-linearities during a blocking force test is the strong irreversibility of the response of the material during loading and unloading, as illustrated by Fig. 18. Fig. 18(a) shows that the difference in the level of strain between the loading and unloading sequence is of

the same order of magnitude as the differences observed for a change in electric field of 0.5 kV/mm. This irreversibility is well correlated to domain switching as already shown by Fig. 15 above. This observation highlights the necessity of a very well defined experimental procedure when measuring macroscopic blocking stress curves, the results being dependent on the path chosen for the application of the external loading.[2] This irreversibility adds to the complexity of the blocking force test.

F. Phase change

An additional source of non-linearity for a composition near to the morphotropic phase boundary is the possible occurrence of phase transformation during the application of the external loading. Such a phase transformation has been observed for the material of this study under the application of high compressive stress.[26] Fig. 19 shows the {200} and {111} peak profiles for $\psi = 0$ under no applied electric field and for several levels of compressive stress. At 122 MPa, a shoulder is clearly formed on the {111} peak indicating the development of a rhombohedral phase. This phase change is

FIG. 18. Irreversibilities during the blocking force test. (a) {200} blocking stress curves obtained for $\psi = 0$ at 1 and 2 kV/mm (a) and (b) {200}, {110}, and {111} blocking stress curves obtained for $\psi = 0$ at 2 kV/mm. Experimental measurements (markers) and approximate evolution for eye guidance (lines). (a) {200} blocking stress curves and (b) {200}, {110}, and {111} blocking stress.
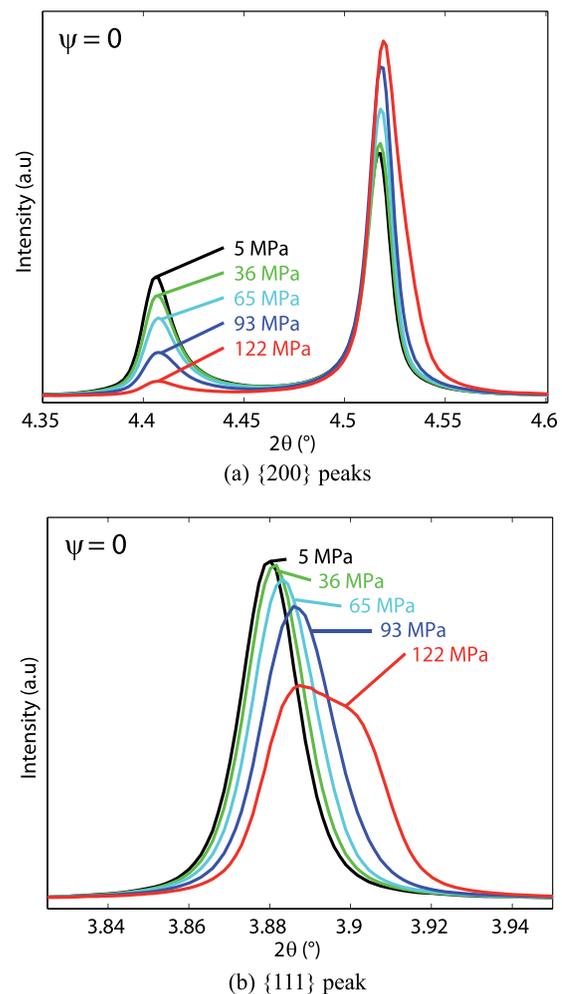
FIG. 19. Diffraction patterns for PZT51-49 under compressive stress from 36 to 122 MPa (no applied electric field) for $\psi = 0$. The pattern at 122 MPa reveals a phase change under stress for the material. (a) {200} peaks and (b) {111} peak.

less evident on the {200} profiles but can be detected on the abnormal broadening of the (200) peak. Would such a phase change occur during a blocking force test, the linear interpretation of the measurements would obviously be at risk. Due to the small level of compressive stress experienced by the material in the experiment reported in this study, no phase change was observed during the blocking force experiments described above.

V. CONCLUSION

A blocking force test has been carried out on a tetragonal PZT piezoelectric ceramic. High energy x-ray diffraction patterns have been recorded *in-situ* in order to provide a local analysis of this experiment. The experiment has been shown to be more complex than often described and several conclusions have been drawn from the analysis:

- The first is that the application of a compressive stress cannot generally cancel the effect of the electric field. The longitudinal strain is suppressed at the macroscopic scale, but heterogeneity remains at the local grain scale. Moreover, the other components of the piezoelectric strain tensor are generally not cancelled by the application of the compressive stress, either at the macroscopic or at the grain scale.
- This complexity can be exploited to identify not only the macroscopic longitudinal piezoelectric coefficient d_{33} and Young's modulus Y but also the macroscopic transverse piezoelectric coefficient d_{31} and the Poisson's ratio ν.
- If analysed from a local perspective, at the grain scale, the test is rich in information. On the grounds of linear piezoelectricity, the local analysis allows the identification of single crystal material parameters regarding piezoelectric and elastic behaviour. The analysis has been performed here under the assumption of uniform electric field and stress within the material and more precise micromechanical tools, such as a self-consistent approach,[14,28] would be necessary to obtain more accurate results.
- It is also shown that macroscopic blocking stress curves can be constructed from the averaging of local strains. The approach allows the identification of apparent material parameters that can be used for the purpose of macroscopic modelling. Here again, advanced micro-mechanical approaches are required to obtain more quantitative information.

However, the linear interpretation can be misleading in some cases. Indeed, piezoelectric behaviour results from a subtle combination of intrinsic piezoelectricity, domain switching, and elasticity through the role of internal stresses. If a significant amount of domain switching is at play during the experiment, the linear interpretation cannot be reasonably applied except for obtaining approximative apparent coefficients. For the tetragonal material tested in this study, it is shown that the source of non-linearities are numerous and that domain switching plays a preponderant role. A high level of intragranular stresses was also identified. The dominant mechanisms can be very different from one material to

another, but high energy x-ray diffraction combined with micro-mechanical modelling can provide powerful tools to characterise the properties of ferroelectric materials.

APPENDIX A: EXAMPLE OF DIFFRACTION PROFILES

A selection of diffraction patterns obtained during the experiment for the {200} and {111} peaks are presented in Figs. 20 and 21. The single {111} peak and split {200} peaks are typical for a tetragonally distorted perovskite ferroelectric. Fig. 20 shows the evolution of the diffraction profiles during the first poling loading, corresponding to the line from point A to point B in Fig. 3. The profiles are given for $\psi = 0$ (parallel to the electric field) and $\psi = 90°$ (perpendicular to the electric field). For $\psi = 0$, increasing electric field strength caused a shift of the {111} peak to smaller 2θ values, caused by an increasing tensile lattice strain, while the (002) peak intensity was significantly enhanced relative to that of the (200) peak due to ferroelectric domain switching towards the poling direction. The opposite trends were observed for $\psi = 90°$, indicating the development of a compressive strain and ferroelectric domain switching away from the transverse directions.

Fig. 21 shows the evolution of the diffraction profiles during the application of a compressive stress under constant electric field (2.5 kV/mm), corresponding to the line from point C to point D in Fig. 3. The profiles are also given for $\psi = 0$ (parallel to the electric field) and $\psi = 90°$ (perpendicular to the electric field). The application of a uniaxial compressive stress along the macroscopic polar axis has little effect on the measured profiles. A slight shift of the (111) peak to higher 2θ values caused by compressive strain is observed for $\psi = 0$. A very small change in the relative intensities of the (002) and (200) peaks can also be noticed for $\psi = 0$, suggesting a small amount of ferroelastic domain switching for applied stresses in the range -5 to -40 MPa, particularly under a static electric field. For $\psi = 90°$, the diffraction profiles seems to be insensitive to the applied stress for this range of applied stress at this level of electric field.
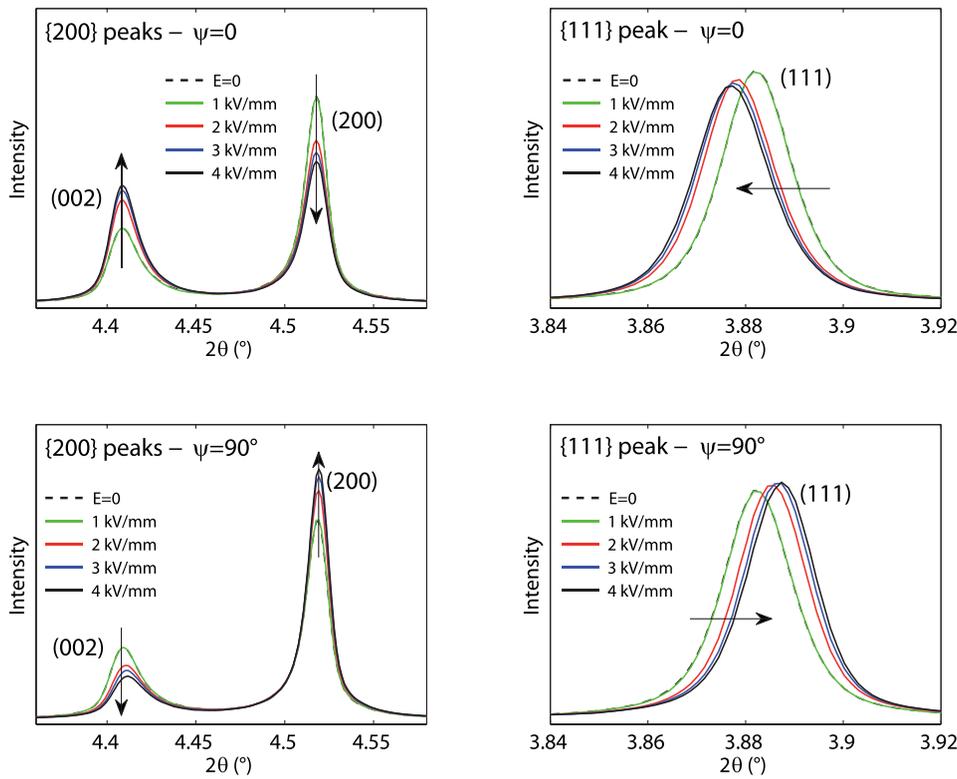
FIG. 20. Diffraction patterns for the first electric field loading (points A–B in Fig. 3): {111} and {200} peaks for $\psi = 0°$ and $\psi = 90°$. The profiles are given for $E = 0$, 1, 2, 3, and 4 kV/mm.
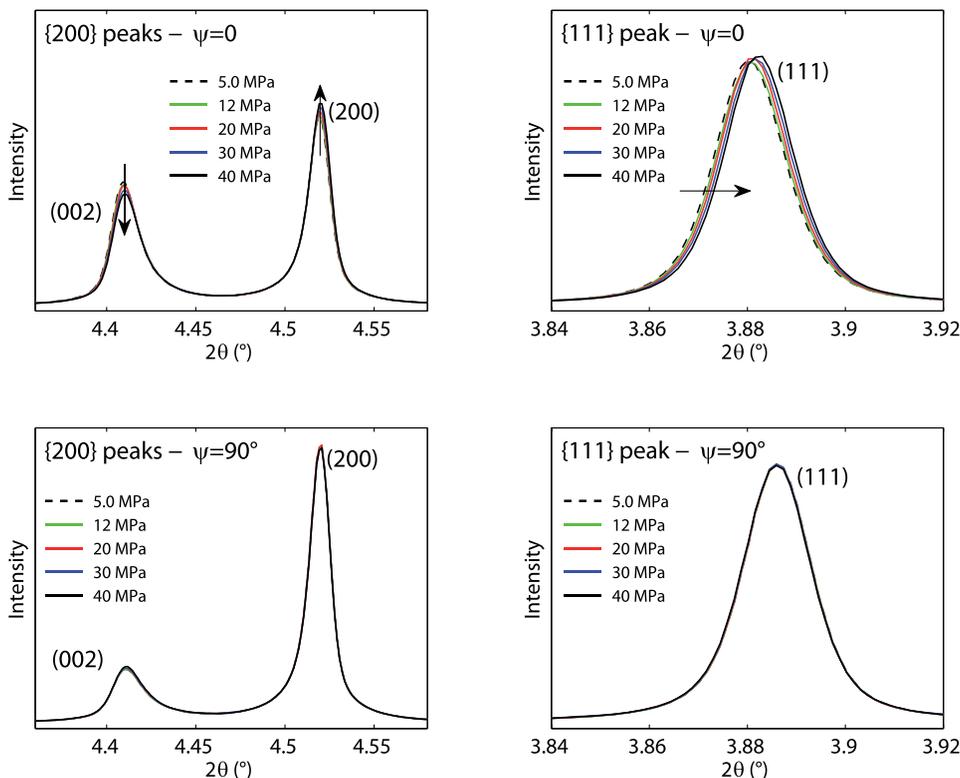
FIG. 21. Diffraction patterns for the last stress loading (points C–D in Fig. 3): {111} and {200} peaks for $\psi = 0$ and $\psi = 90°$. The patterns show very little domain switching under stress. The profiles are given for $\sigma = 5.0$, 12, 20, 30, and 40 MPa.

APPENDIX B: PEAK POSITION MONITORING—RAW DATA

The evolution of (002) and (200) lattice spacings during the course of the experiment is presented in Figs. 22 and 23, respectively. The sketch on the right shows the orientation of the crystal unit cell with respect to the macroscopic loading.

The error bar obtained from the unpoled state ($\pm 3 \times 10^{-4}$ Å for the {200} orientations) is also indicated on the graphs. The typical peak fitting error for a given ψ value, not represented in the figures, was lower than 10^{-5} Å. Fig. 22 gives the evolution of the c-axis of the tetragonal unit cell for $\psi = 0$ and $\psi = 90°$. It can be noticed that the overall level of
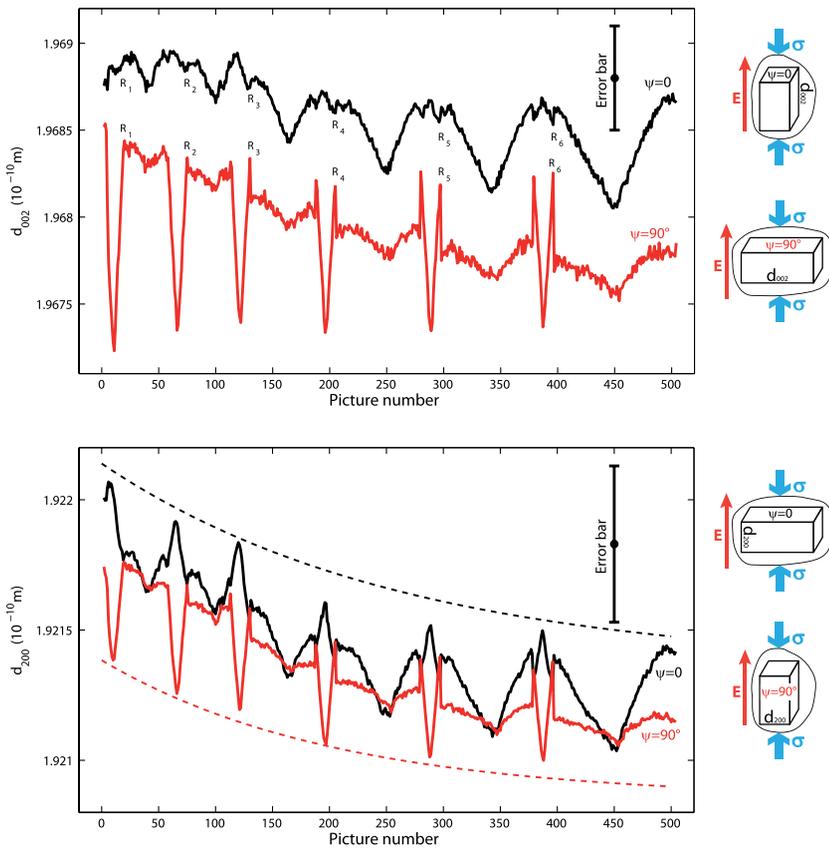
FIG. 22. Evolution of d_{002} (c-axis) during the *in-situ* experiment, $\psi = 0°$ (top) and $\psi = 90°$ (bottom). The sketch on the right depicts the orientation of the crystal structure with respect to the macroscopic loading. The error bar gives the variability observed between the different azimuthal directions, taken as the uncertainty on the absolute value of the lattice spacing ($\pm 3 \times 10^{-4}$ Å here, see Table I). As evident from the graph, the changes in the value of d_{002} are obtained with a much higher resolution. For example, the typical peak fitting error for a given ψ value was lower than 10^{-5} Å.
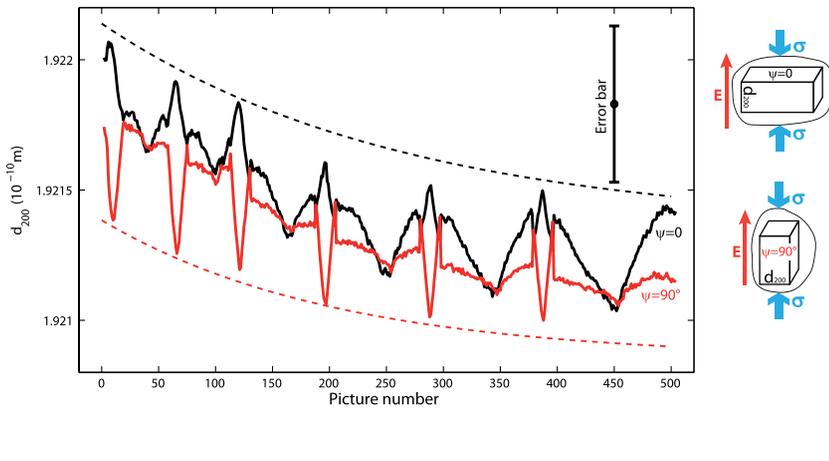
FIG. 23. Evolution of d_{200} (a-axis) during the *in-situ* experiment, $\psi = 0°$ (top) and $\psi = 90°$ (bottom). The sketch on the right depicts the orientation of the crystal structure with respect to the macroscopic loading. The error bar gives the variability observed between the different azimuthal directions, taken as the uncertainty on the absolute value of the lattice spacing ($\pm 3 \times 10^{-4}$ Å here, see Table I). As evident from the graph, the changes in the value of d_{200} are obtained with a much higher resolution. The dashed line reflects the drift observed during the course of the experiment. The black and red line (top and bottom, respectively) are obtained from the results $\psi = 0°$ and $\psi = 90°$ taken independently.

variation of d_{002} is relatively small during the course of the experiment, nearly within the range of the error bar. Fig. 23 gives the evolution of the a-axis of the tetragonal structure for $\psi = 0$ and $\psi = 90°$. The variations observed for d_{200} are very small and lie within the range of the error bar. For this orientation, the a-axis could almost be considered as constant. A progressive drift of the value is observed. This drift has been fitted separately on the curves for $\psi = 0$ and $\psi = 90°$ by taking as reference the values at maximum field (4 kV/mm) and the values just after repoling. The drift was found to be very similar on both curves as illustrated by the dashed lines in Fig. 23.

Similar drifts are found for the other lattice spacings but are less visible due to the larger variations obtained. The evolution of the {111} lattice spacings during the course of the experiment is presented in Fig. 24. The corresponding peak is a single peak so that the crystallographic orientation can be considered without considering the local polarisation orientation. The levels of variation are also much higher than for a- and c-axis, as shown by the error bar. The analysis of the evolution of the lattice spacings is detailed in the article from the strain curves presented in Figs. 5 and 16.
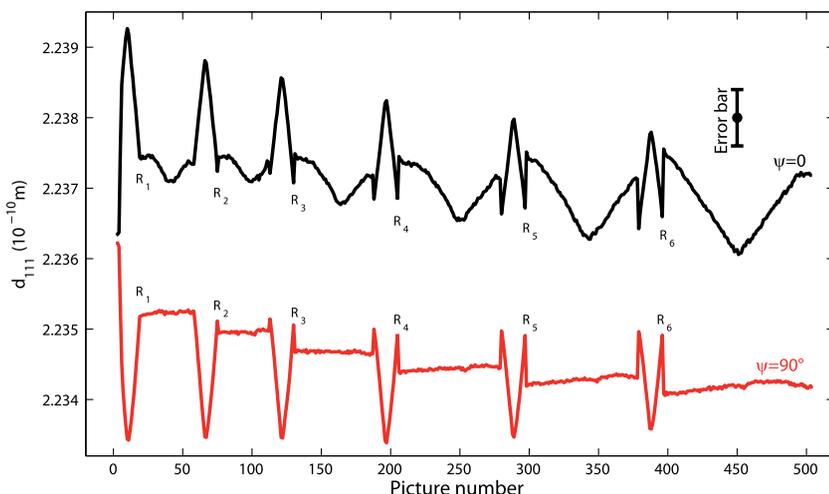
FIG. 24. Evolution of d_{111} during the *in-situ* experiment, $\psi = 0°$ (top) and $\psi = 90°$ (bottom). The errorbar gives the variability observed between the different azimuthal directions, taken as the uncertainty on the absolute value of the lattice spacing ($\pm 4 \times 10^{-4}$ Å here, see Table I). As evident from the graph, the changes in the value of d_{111} are obtained with a much higher resolution. For example, the typical peak fitting error for a given ψ value was lower than 10^{-5} Å.

APPENDIX C: ELASTIC AND PIEZOELECTRIC STRAIN FOR A TETRAGONAL SINGLE CRYSTAL

In the coordinate system associated with the tetragonal single crystal, the piezoelectric coefficient tensor **d** is expressed as

$$\mathbf{d} = \begin{pmatrix} 0 & 0 & 0 & 0 & d_{15} & 0 \\ 0 & 0 & 0 & d_{15} & 0 & 0 \\ d_{31} & d_{31} & d_{33} & 0 & 0 & 0 \end{pmatrix}. \qquad (C1)$$

Assuming a cubic symmetry, the elastic compliance tensor $\mathcal{S}^E$ is expressed—in Voigt notation—as

$$\mathcal{S}^E = \begin{pmatrix} S_{11} & S_{12} & S_{12} & 0 & 0 & 0 \\ S_{12} & S_{11} & S_{12} & 0 & 0 & 0 \\ S_{12} & S_{12} & S_{11} & 0 & 0 & 0 \\ 0 & 0 & 0 & S_{44} & 0 & 0 \\ 0 & 0 & 0 & 0 & S_{44} & 0 \\ 0 & 0 & 0 & 0 & 0 & S_{44} \end{pmatrix}. \qquad (C2)$$

The macroscopic direction **z** (Fig. 25) is given by

$$\mathbf{z} = \begin{bmatrix} \sin\varphi\cos\theta \\ \sin\varphi\sin\theta \\ \cos\varphi \end{bmatrix}. \qquad (C3)$$

The directions **p** to the vertical direction **z**, parametrised with an angle α to define their orientation in the plane perpendicular to **z** are given by

$$\mathbf{p}(\alpha) = \begin{bmatrix} -\cos\alpha\cos\varphi\cos\theta + \sin\alpha\sin\theta \\ -\cos\alpha\cos\varphi\sin\theta - \sin\alpha\cos\theta \\ \cos\alpha\sin\varphi \end{bmatrix}. \qquad (C4)$$

1. Piezoelectric strain

If a local electric field of amplitude E is applied along direction **z**, the piezoelectric strain $\boldsymbol{\varepsilon}^{pz}$ is defined by
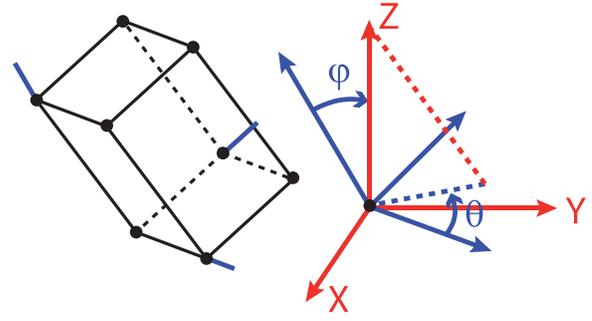
FIG. 25. Definition of the angles ψ and θ for the orientation of the crystal structure.

$$\boldsymbol{\varepsilon}^{pz} = {}^t\mathbf{d}.E\mathbf{z}$$

$$= \begin{pmatrix} d_{31}\cos\varphi & 0 & \dfrac{1}{2}d_{15}\sin\varphi\cos\theta \\[2mm] 0 & d_{31}\cos\varphi & \dfrac{1}{2}d_{15}\sin\varphi\sin\theta \\[2mm] \dfrac{1}{2}d_{15}\sin\varphi\cos\theta & \dfrac{1}{2}d_{15}\sin\varphi\sin\theta & d_{33}\cos\varphi \end{pmatrix} E. \qquad (C5)$$

The strain $\varepsilon_{//}^{pz}$ measured in the direction parallel to the electric field is

$$\varepsilon_{\parallel}^{pz} = {}^t\mathbf{z}\cdot\boldsymbol{\varepsilon}^{pz}\cdot\mathbf{z} = (d_{33}\cos^2\varphi + (d_{31}+d_{15})\sin^2\varphi)E\cos\varphi. \qquad (C6)$$

The strain $\varepsilon_{\perp}^{pz}$ measured in a direction perpendicular to the electric field is

$$\varepsilon_{\perp}^{pz}(\alpha) = {}^t\mathbf{p}.\boldsymbol{\varepsilon}^{pz}.\mathbf{p}$$
$$= (d_{31} + (d_{33}-d_{31}-d_{15})\cos^2\alpha\sin\varphi)E\cos\varphi. \qquad (C7)$$

TABLE IX. Local piezoelectric strain as a function of the orientation (φ, θ) of the local electric field with respect to the poling direction [001]. Both the components parallel $\varepsilon_{\parallel}^{pz}$ and perpendicular $\varepsilon_{\perp}^{pz}$ to the electric field are given. The perpendicular component is parametrised by an angle α, since the perpendicular direction is not uniquely defined by the azimuthal direction. For the orientations $\psi = 90°$ parallel to [101] and [111], there is no simple expression of z using the chosen parametrisation $(\varphi, \theta, \alpha)$ so that the corresponding expressions have been defined using the directions $\mathbf{z}_{p101}$ and $\mathbf{z}_{p111}$, respectively, with $\mathbf{z}_{p101} = \left[-\dfrac{\sin\beta}{\sqrt{2}};\ \cos\beta;\ \dfrac{\sin\beta}{\sqrt{2}}\right]$ and $\mathbf{z}_{p111} = \left[-\dfrac{\cos\beta}{\sqrt{2}}-\dfrac{\sin\beta}{\sqrt{6}};\ \dfrac{\cos\beta}{\sqrt{2}}-\dfrac{\sin\beta}{\sqrt{6}};\ \dfrac{2\sin\beta}{\sqrt{6}}\right]$ and $\beta \in [0\,2\pi]$.

Orientation	$(\varphi, \theta, \alpha)$	$\varepsilon_{\parallel}^{pz}$	$\varepsilon_{\perp}^{pz}$
$[hkl]$ // $(\psi=0)$	$(\varphi, \theta, \alpha)$	(C6)	(C7)
$[hk0]$ // $(\psi=0)$	$(90°, \theta, \alpha)$	0	0
$[001]$ // $(\psi=0)$	$(0, \theta, \alpha)$	$d_{33}E$	$d_{31}E$
$[100]$ // $(\psi=0)$	$(90°, 0, \alpha)$	0	0
$[101]$ // $(\psi=0)$	$(45°, 0, \alpha)$	$\dfrac{1}{2\sqrt{2}}(d_{33}+d_{31}+d_{15})E$	$\left(\dfrac{d_{31}}{\sqrt{2}}+\dfrac{1}{2}(d_{33}-d_{31}-d_{15})\cos^2\alpha\right)E$
$[110]$ // $(\psi=0)$	$(90°, 45°, \alpha)$	0	0
$[111]$ // $(\psi=0)$	$(54.7°, 45°, \alpha)$	$\dfrac{1}{3\sqrt{3}}(d_{33}+2d_{31}+2d_{15})E$	$\left(\dfrac{d_{31}}{\sqrt{3}}+\dfrac{\sqrt{2}}{3}(d_{33}-d_{31}-d_{15})\cos^2\alpha\right)E$
$[001]$ // $(\psi=90°)$	$(90°, \theta, 0)$	0	0
$[100]$ // $(\psi=90°)$	$(\varphi, 90°, 90°)$	(C6)	$d_{31}E\cos\varphi$
$[101]$ // $(\psi=90°)$	$\mathbf{z}_{p101}$	$\dfrac{1}{2\sqrt{2}}E\sin\beta[d_{33}+d_{31}-(d_{33}-d_{31}-2d_{15})\cos^2\beta]$	$\dfrac{1}{2\sqrt{2}}(d_{33}+d_{31}-d_{15})E\sin\beta$
$[110]$ // $(\psi=90°)$	$(\varphi, 135°, 90°)$	(C6)	$d_{31}E\cos\varphi$
$[111]$ // $(\psi=90°)$	$\mathbf{z}_{p111}$	$\dfrac{1}{\sqrt{6}}\left[\dfrac{2\sin^2\beta}{3}(2d_{33}-d_{31}-d_{15})+d_{31}+d_{15}\right]E\sin\beta$	$\dfrac{2}{3\sqrt{6}}(d_{33}+2d_{31}-d_{15})E\sin\beta$

The results for both $\varepsilon_\parallel^{pz}$ and $\varepsilon_\perp^{pz}$ do not depend on θ but only on the angle φ between the electric field and the local poling direction. Several particular cases for the electric field orientation are summarised in Table IX. If the electric field is applied along the poling direction ($\varphi = 0$), $\varepsilon_\parallel^{pz} = d_{33}E$ and $\varepsilon_\perp^{pz} = d_{31}E$ corresponding to the usual longitudinal mode, and if the electric field is applied perpendicular the poling direction ($\varphi = 90°$), $\varepsilon_\parallel^{pz} = \varepsilon_\perp^{pz} = 0$ corresponding to shear mode.

2. Apparent piezoelectric coefficients

If an electric field of amplitude E along a direction [hkl] is applied to a single crystal it will deform according to (C6) and (C7). The apparent longitudinal piezoelectric coefficient d_l and apparent transverse piezoelectric coefficient d_t can be defined as

$$d_l = \frac{\varepsilon_\parallel^{pz}}{E} \quad \text{and} \quad d_t = \frac{\varepsilon_\perp^{pz}}{E}. \tag{C8}$$

An average transverse piezoelectric coefficient can be obtained for an orientation of the electric field by integrating the expression of $\varepsilon_\perp^{pz}$ for $\alpha \in [0, 2\pi]$. The apparent piezoelectric coefficient for a single crystal loaded in any direction $\mathbf{z}$ can then be deduced from the expressions listed in Table IX.

3. Elastic strain

Consider a uniaxial stress of amplitude σ applied along the direction $\mathbf{z}$. The stress tensor $\boldsymbol{\sigma}$ can be expressed in the crystal coordinate system as

$$\boldsymbol{\sigma} = \sigma\, \mathbf{z} \otimes \mathbf{z} = \begin{pmatrix} \sin^2\varphi \cos^2\theta & \sin^2\varphi \cos\theta \sin\theta & \cos\varphi \sin\varphi \cos\theta \\ \sin^2\varphi \cos\theta \sin\theta & \sin^2\varphi \sin^2\theta & \cos\varphi \sin\varphi \sin\theta \\ \cos\varphi \sin\varphi \cos\theta & \cos\varphi \sin\varphi \sin\theta & \cos^2\varphi \end{pmatrix} \sigma. \tag{C9}$$

The corresponding elastic strain $\boldsymbol{\varepsilon}^e$ is given by Hooke's law

$$\boldsymbol{\varepsilon}^e = \mathcal{S}^E : \boldsymbol{\sigma} = S_{11}\sigma \begin{pmatrix} \sin^2\varphi \cos^2\theta & 0 & 0 \\ 0 & \sin^2\varphi \sin^2\theta & 0 \\ 0 & 0 & \cos^2\varphi \end{pmatrix} + S_{12}\sigma \begin{pmatrix} \sin^2\varphi \sin^2\theta + \cos^2\varphi & 0 & 0 \\ 0 & \sin^2\varphi \cos^2\theta + \cos^2\varphi & 0 \\ 0 & 0 & \sin^2\varphi \end{pmatrix}$$

$$+ \frac{1}{2}S_{44}\sigma \begin{pmatrix} 0 & \sin^2\varphi \cos\theta \sin\theta & \cos\varphi \sin\varphi \cos\theta \\ \sin^2\varphi \cos\theta \sin\theta & 0 & \cos\varphi \sin\varphi \sin\theta \\ \cos\varphi \sin\varphi \cos\theta & \cos\varphi \sin\varphi \sin\theta & 0 \end{pmatrix} \tag{C10}$$

The strain $\varepsilon_{//}^e$ measured in the direction parallel to the stress is

TABLE X. Local elastic strain as a function of the orientation (φ, θ) of the uniaxial compressive stress with respect to the poling direction [001]. Both the components parallel $\varepsilon_\parallel^{pz}$ and perpendicular $\varepsilon_\perp^{pz}$ to the electric field are given. The perpendicular component is parametrised by an angle α, since the perpendicular direction is not uniquely defined by the azimuthal direction. For the orientations $\psi = 90°$ parallel to [111], there is no simple expression of z using the chosen parametrisation (φ, θ, α) so that the corresponding expressions have been defined using the directions $\mathbf{z}_{p111}$ with $\mathbf{z}_{p111} = \left[-\frac{\cos\beta}{\sqrt{2}} - \frac{\sin\beta}{\sqrt{6}}; \frac{\cos\beta}{\sqrt{2}} - \frac{\sin\beta}{\sqrt{6}}; \frac{2\sin\beta}{\sqrt{6}} \right]$ and $\beta \in [0\,2\pi]$.

Orientation	$(\varphi, \theta, \alpha)$	$\varepsilon_\parallel^e$	$\varepsilon_\perp^e$
$[hkl]$ ($\psi = 0$)	$(\varphi, \theta, \alpha)$	(C11)	(C12)
$\langle 100 \rangle$ ($\psi = 0$)	$(0, \theta, \alpha)$	$S_{11}\sigma$	$S_{12}\sigma$
$\langle 110 \rangle$ ($\psi = 0$)	$(90°, 45°, \alpha)$	$\frac{\sigma}{4}(2S_{11} + 2S_{12} + S_{44})$	$\left[\frac{1}{2}S_{12} + \frac{\sin^2\alpha}{4}(2S_{11} + 2S_{12} - S_{44}) \right]\sigma$
$\langle 111 \rangle$ ($\psi = 0$)	$(54.7°, 45°, \alpha)$	$\frac{\sigma}{3}(S_{11} + 2S_{12} + S_{44})$	$\frac{\sigma}{6}(2S_{11} + 4S_{12} - S_{44})$
$\langle 100 \rangle$ ($\psi = 90°$)	$(\varphi, 90°, 90°)$	$\sigma[(S_{11}(\cos^4\varphi + \sin^4\varphi) + (2S_{12} + S_{44})\cos^2\varphi \sin^2\varphi]$	$S_{12}\sigma$
$\langle 110 \rangle$ ($\psi = 90°$)	$(\varphi, 135°, 90°)$	$\sigma\left[\left(S_{11}\left(\cos^4\varphi + \frac{1}{2}\sin^4\varphi\right) + (2S_{12} + S_{44})\sin^2\varphi\left(1 - \frac{3}{4}\sin^2\varphi\right) \right) \right]$	$\left[S_{12} + \frac{\sin^2\varphi}{4}(2S_{11} - 2S_{12} - S_{44}) \right]\sigma$
$\langle 111 \rangle$ ($\psi = 90°$)	$\mathbf{z}_{p111}$	$(2S_{11} + 2S_{12} + S_{44})\frac{\sigma}{4}$	$(2S_{11} + 4S_{12} - S_{44})\frac{\sigma}{6}$

$$\varepsilon_\parallel^e = {}^t\mathbf{z} \cdot \boldsymbol{\varepsilon}^e \cdot \mathbf{z} = S_{11}\,\sigma\,(\sin^4\varphi\cos^4\theta + \sin^4\varphi\sin^4\theta + \cos^4\varphi)$$
$$+ (2S_{12} + S_{44})\,\sigma\,\sin^2\varphi\,(\sin^2\varphi\cos^2\theta\sin^2\theta + \cos^2\varphi). \tag{C11}$$

The strain $\varepsilon_\perp^e$ measured in a direction perpendicular to the stress is

$$\varepsilon_\perp^e(\alpha) = {}^t\mathbf{p} \cdot \boldsymbol{\varepsilon}^e \cdot \mathbf{p}$$
$$= S_{11}\,\sigma\,\sin^2\varphi\,[\cos^2\alpha\cos^2\varphi(1 + \cos^4\theta + \sin^4\theta)$$
$$- 2\cos\alpha\sin\alpha\cos\varphi\cos\theta\sin\theta(\cos^2\theta - \sin^2\theta)$$
$$+ 2\sin^2\alpha\cos^2\theta\sin^2\theta]$$
$$+ S_{12}\,\sigma\,[\cos^2\alpha\,(2\cos^2\varphi\sin^2\varphi\cos^2\theta\sin^2\theta$$
$$+ \cos^4\varphi + \sin^4\varphi) + 2\cos\alpha\sin\alpha\cos\varphi$$
$$\times \sin^2\varphi\cos\theta\sin\theta(\cos^2\theta - \sin^2\theta)$$
$$+ \sin^2\alpha(1 - 2\sin^2\varphi\cos^2\theta\sin^2\theta)]$$
$$+ S_{44}\,\sigma\,\sin^2\varphi\,[\cos^2\alpha\cos^2\varphi(\cos^2\theta\sin^2\theta - 1)$$
$$+ \cos\alpha\sin\alpha\cos\varphi\cos\theta\sin\theta(\cos^2\theta - \sin^2\theta)$$
$$- \sin^2\alpha\cos^2\theta\sin^2\theta]. \tag{C12}$$

Several particular cases for the electric field orientation are summarised in Table X.

4. Apparent elastic coefficients

If a stress of amplitude σ along a direction [hkl] is applied to a single crystal it will deform according to (C11) and (C12). The apparent longitudinal (Young's) and transverse modulus Y and $Y_\perp$ can be defined as

$$Y = \frac{\sigma}{\varepsilon_{\parallel(\psi=0)}^e} \quad \text{and} \quad Y_\perp = \frac{\sigma}{\varepsilon_{\perp(\psi=90^o)}^e}. \tag{C13}$$

Average coefficients can be obtained for a given orientation by integrating the expression of $\varepsilon_\parallel^e$ or $\varepsilon_\perp^e$ within $[0, 2\pi]$. The apparent elastic coefficient for a single crystal loaded in any direction $\mathbf{z}$ can then be deduced from the expressions listed in Table X.

[1] D. Damjanovic, Rep. Prog. Phys. **61**, 1267–1324 (1998).
[2] K. G. Webber, D. J. Franzbach, and J. Koruza, J. Am. Ceram. Soc. **97**(9), 2842–2849 (2014).
[3] D. A. Hall, A. Steuwer, B. Cherdhirunkorn, P. J. Withers, and T. Mori, J. Mech. Phys. Solids **53**, 249–260 (2005).
[4] A. Pramanick, D. Damjanovic, J. E. Daniels, J. C. Nino, and J. L. Jones, J. Am. Ceram. Soc. **94**, 293–309 (2011).
[5] D. A. Hall, A. Steuwer, B. Cherdhirunkorn, T. Mori, and P. J. Withers, J. Appl. Phys. **96**, 4245–4252 (2004).
[6] D. A. Hall, A. Steuwer, B. Cherdhirunkorn, T. Mori, and P. J. Withers, Acta Mater. **54**, 3075–3083 (2006).
[7] J. L. Jones, E. B. Slamovich, and K. J. Bowman, J. Appl. Phys. **97**, 034113 (2005).
[8] J. L. Jones, B. J. Iverson, and K. J. Bowman, J. Am. Ceram. Soc. **90**, 2297–2314 (2007).
[9] K. A. Schönau, M. Knapp, H. Kungl, M. J. Hoffmann, and H. Fuess, Phys. Rev. B **76**, 144112 (2007).
[10] A. K. Singh, S. K. Mishra, Ragini, D. Pandey, S. Yoon, S. Baik, and N. Shin, Appl. Phys. Lett. **92**, 022910 (2008).
[11] A. Pramanick, J. E. Daniels, and J. L. Jones, J. Am. Ceram. Soc. **92**, 2300–2310 (2009).
[12] J. E. Daniels, W. Jo, J. Rödel, V. Honkimäki, and J. L. Jones, Acta Mater. **58**, 2103–2111 (2010).
[13] W. Jo, R. Dittmer, M. Acosta, J. Zang, C. Groh, E. Sapper, K. Wang, and J. Rödel, J. Electroceram. **29**, 71–93 (2012).
[14] L. Daniel, D. A. Hall, K. G. Webber, A. King, and P. J. Withers, J. Appl. Phys. **115**, 174102 (2014).
[15] R. Dittmer, K. G. Webber, E. Aulbach, W. Jo, X. Tan, and J. Rödel, Sens. Actuators, A **189**, 187–194 (2013).
[16] K. G. Webber, E. Aulbach, and J. Rödel, J. Phys. D: Appl. Phys. **43**, 365401 (2010).
[17] Y. H. Seo, A. Bencan, J. Koruza, B. Malic, M. Kosec, and K. G. Webber, J. Am. Ceram. Soc. **94**(12), 4419–4425 (2011).
[18] A. P. Hammersley, ESRF Internal Report No. ESRF98HA01T, FIT2D V9.129 Reference Manual V3.1, 1998.
[19] A. P. Hammersley, S. O. Svensson, M. Hanfland, A. N. Fitch, and D. Häusermann, High Pressure Res. **14**, 235–248 (1996).
[20] See http://admet.com/products/universal-testing-machines/ for a description of the loading device.
[21] D. Faurie, O. Castelnau, R. Brenner, P. O. Renault, E. Le Bourhis, and Ph. Goudeau, J. Appl. Crystallogr. **42**, 1073–1084 (2009).
[22] M. R. Daymond, J. Appl. Phys. **96**(8), 4263–4272 (2004).
[23] J. E. Daniels, T. R. Finlayson, A. J. Studer, M. Hoffman, and J. L. Jones, J. Appl. Phys. **101**, 094104 (2007).
[24] Y. H. Seo, J. Koruza, A. Bencan, B. Malic, J. Rödel, and K. G. Webber, J. Am. Ceram. Soc. **97**(5), 1582–1588 (2014).
[25] *Piezoelectric and Acoustic Materials for Transducer Applications*, edited by A. Safari and E. Koray Akdoğan (Springer, 2008).
[26] Y. H. Seo, D. J. Franzbach, J. Koruza, A. Bencan, B. Malic, M. Kosec, J. L. Jones, and K. G. Webber, Phys. Rev. B **87**, 094116 (2013).
[27] L. Daniel, D. A. Hall, and P. J. Withers, Mech. Mater. **71**, 85–100 (2014).
[28] R. Corcolle, L. Daniel, and F. Bouillault, Phys. Rev. B **78**(21), 214110 (2008).